*remote sensing*

MDPI

*Article*

# Sequential Multimodal Underwater Single-Photon Lidar Adaptive Target Reconstruction Algorithm Based on Spatiotemporal Sequence Fusion

**Tian Rong [1], Yuhang Wang [2], Qiguang Zhu [2], Chenxu Wang [1,3,*], Yanchao Zhang [3], Jianfeng Li [3], Zhiquan Zhou [3] and Qinghua Luo [3]**

[1] Aerospace College, Harbin Institute of Technology, Harbin 150001, China; 22b921022@stu.hit.edu.cn
[2] College of Information Science and Engineering, Yanshan University, Qinhuangdao 066000, China; q17863136808@163.com (Y.W.); luoj1379@outlook.com (Q.Z.)
[3] College of Information Science and Engineering, Harbin Institute of Technology (Weihai), Weihai 264209, China; zhangyanchao66@sina.com (Y.Z.); lijianfeng@hit.edu.cn (J.L.); zzq@hitwh.edu.cn (Z.Z.); luoqinghua081519@163.com (Q.L.)
* Correspondence: wangchenxu@hit.edu.cn

**Abstract:** For the demand for long-range and high-resolution target reconstruction of slow-moving small underwater targets, research on single-photon lidar target reconstruction technology is being carried out. This paper reports the sequential multimodal underwater single-photon lidar adaptive target reconstruction algorithm based on spatiotemporal sequence fusion, which has strong information extraction and noise filtering ability and can reconstruct the target depth and reflective intensity information from complex echo photon time counts and spatial pixel relationships. The method consists of three steps: data preprocessing, sequence-optimized extreme value inference filtering, and collaborative variation strategy for image optimization to achieve high-quality target reconstruction in complex underwater environments. Simulation and test results show that the target reconstruction method outperforms the current imaging algorithms, and the built single-photon lidar system achieves underwater lateral and distance resolution of 5 mm and 2.5cm@6AL, respectively. This indicates that the method has a great advantage in sparse photon counting imaging and possesses the capability of underwater target imaging under the background of strong light noise. It also provides a good solution for underwater target imaging of small slow-moving targets with long-distance and high-resolution.

**Keywords:** ocean; optical detection; slow-moving small targets; single-photon lidar; target reconstruction



Academic Editors: Xuebo Zhang, Haiyong Xu, Jingyue Lu, Lei Zhang, Marc Pinto and Farman Ali

Received: 28 November 2024
Revised: 12 January 2025
Accepted: 13 January 2025
Published: 15 January 2025

**Citation:** Rong, T.; Wang, Y.; Zhu, Q.; Wang, C.; Zhang, Y.; Li, J.; Zhou, Z.; Luo, Q. Sequential Multimodal Underwater Single-Photon Lidar Adaptive Target Reconstruction Algorithm Based on Spatiotemporal Sequence Fusion. *Remote Sens.* **2025**, *17*, 295. https://doi.org/10.3390/rs17020295



## 1. Introduction

With the deepening of ocean exploration, long-range and high-resolution imaging of small targets has become the basic technology to support many other ocean exploration techniques and has received great attention [1–7]. Traditional optical detection methods suffer from light attenuation and low contrast in the underwater imaging environment, leading to image quality degradation [8–10]. Current mainstream acoustic detection faces limitations of acoustic wave propagation speed and resolution, as well as problems of signal attenuation and distortion caused by the non-uniformity of seawater medium, which reduces the reliability and practicability [11–13]. The emergence of single-photon lidar provides a new way for underwater detection [14–17], which becomes an effective way

to solve the problem of detecting targets in low-light and high-light attenuation intensity environments, and has aroused extensive research interests.

As the key influencing factors of single-photon lidar, the iteration of imaging algorithms and the improvement of hardware systems complement each other. At present, in the field of single-photon lidar development, many researchers and scholars have made good achievements in the hardware system [15,18–23]. However, in practical applications, photon-level detection sensitivity brings about an improvement in detection capability, while noise-induced photon events also cause a problem of increased noise points and bring about randomness of detection, coupled with a lack of information caused by severe optical attenuation. This interferes with the selection and reconstruction of the target information and ultimately affects the detection results [24–26]. So, robust imaging algorithms are indispensable for single-photon detection systems. According to the differences in imaging mechanisms, data processing means, and technical implementations the existing single-photon lidar imaging algorithms are mainly divided into two major categories, namely, neural network-based imaging approaches [27,28], and imaging algorithms based on traditional modeling approaches [29,30]. The neural network-based approach is able to learn nonlinear mapping relationships from complex data by taking advantage of data driven through deep learning techniques, largely detaching itself from a priori experience and showing excellent imaging results. However, the problems of data dependence, high demand for computational resources, limited generalization ability, and insufficient retention of edge information have seriously developed the single-photon imaging based on neural network imaging approach [31–38]. Modeling-based imaging algorithms have high computational efficiency, flexibility in parameter tuning, strong generalization ability, robustness, and cost-effectiveness and are particularly suitable for applications with limited resources or requiring fast response due to their low computational requirements and easy integration [39–41]. Among the current single-photon imaging methods based on modeling approaches, non-fixed pixel scan-time reconstruction methods, represented by first-photon methods [42,43], first-photon group [44,45], and other "firstness" photon information reconstruction targeting methods, are better in terms of resource optimization, but the data processing is more complicated and the system requirements are higher. Also, the current algorithms are not well adapted to complex environments, especially underwater environments, and the characteristics of manual parameterization [42–48] are difficult to adapt to changing environments. Fixed-pixel acquisition time reconstruction methods, although sacrificing some flexibility and resource efficiency, are suitable for standardized imaging due to their consistency and processing simplicity, and methods such as the sequential two-mode fusion imaging algorithm (STMF) also compensate for the echo signal variability [49]. However, due to median filtering [44,45,50,51] the intrinsic spatial and temporal connections of the single-photon data and the distributional characteristics of the signal are ignored. Also, a large amount of fringe information and high-frequency components are lost, and in underwater environments with severe backscattering, non-localized spatial pixel filtering, which is excellent in filtering performance, loses its robustness. Numerous algorithms are applicable to gaze imaging systems [52–55], which further reduce the spatial resolution and flexibility of single-photon lidar systems and increase their information acquisition cost.

An efficient single-photon lidar imaging algorithm is urgently needed for long-range and high-resolution imaging detection of underwater slow-moving small targets. In this study, we report on the sequential multimodal underwater single-photon lidar adaptive target reconstruction algorithm based on spatiotemporal sequence fusion (SUARF), which is based on the pixel-scanning imaging principle. This takes advantage of the fundamental property that the noise photons in the echo signal are differently distributed with the target

information photons in the temporal histogram in decomposing the pulse-accumulated single-photon raw signal, and with the help of an optimization strategy, it settles the target depth and reflectivity information. Compared with algorithms such as the STMF and the first photon group with excellent imaging performance, this method does not require manual parameter adjustment and can efficiently accomplish the target reconstruction task under a variety of challenging imaging conditions, which can provide technical support for underwater target imaging detection.

Our main technical innovations and contributions are as follows:

- We propose the SUARF algorithm consisting of data preprocessing, sequence optimized maximum value inference filtering, and collaborative variation strategy for image optimization to effectively extract target depth and reflection intensity information from complex echo photon time counting. The mask and pixel summation operations are used for data preprocessing to remove the strong backscattering of water near the LiDAR glass window and part of the system noise. Sequence optimization maximum inference filtering combined with matching filter and maximum group filtering can accurately select target depth-reflection information. The collaborative variation strategy integrates the adaptive Wiener–Hopf filter and global morphological constraint into the total variational smoothing constraint to enhance the overall smoothness and effectively deal with abnormal pixel values.
- We built an underwater single-photon LiDAR prototype for testing. The results show that compared with the latest scanning single-photon LiDAR imaging algorithm, the (SSIM, RMSE) of the depth and reflection intensity map was improved by (15%, 57%) and (48%, 71%), respectively. We also proposed an evaluation index $R_T$ to comprehensively evaluate the depth-reflection intensity of the SSIM and RMSE index, which was improved by 24%. All results show that the proposed algorithm has good scene reconstruction performance.

## 2. SUARF Target Reconstruction Algorithm Model

The SUARF algorithm consists of three steps: data preprocessing, sequence-optimized extreme value inference filtering, and collaborative variation strategy for image optimization to achieve high-quality target reconstruction in complex underwater environments. The schematic diagram of the SUARF algorithm is as in Figure 1.

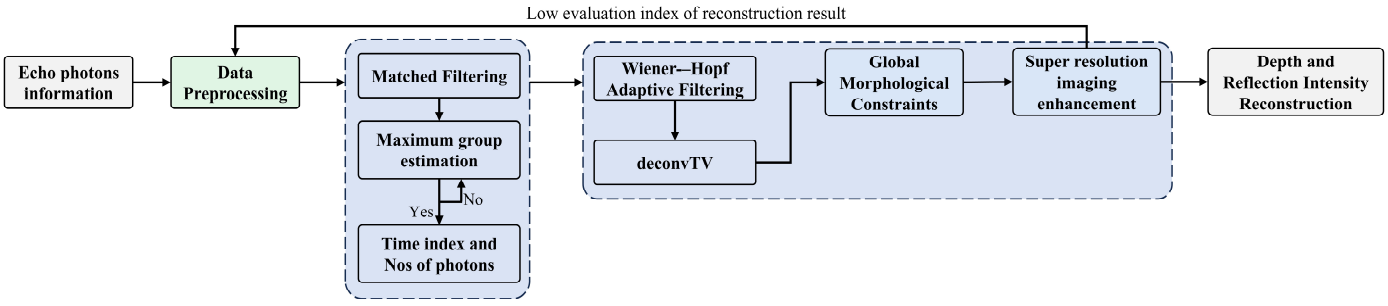


**Figure 1.** SUARF target reconstruction algorithm flow diagram.

In the original signal of single-photon lidar, the arrival moments of signal photons will be centrally distributed on the time axis. The noise photons do not carry any information about the target, and are independent of each other with respect to the arrival moments of the signal photons, and thus are uniformly distributed in the detection period. According to the above characteristics, the signal photons and noise photons can be initially decomposed using sequence-optimized extreme value inference filtering, and then the outliers can be filtered out using the collaborative variation strategy, while the global morphological

constraints can be used to maintain the structural features. The flowchart of the algorithm is shown in Algorithm 1.

**Algorithm 1** Overall framework: SUARF

**Input:** Photons echo data

**Output:** Depth and Reflection Intensity Information

/// First Step:
(1)Data coordinate conversion
(2)Data cleaning ← Select the mask

// Second Step:
$y(t) = s^*(-t) \quad r(t)$ // Matched filtering
**while** $(x, y) \in (X, Y)$ **do**
  **if** *G is the largest photons group* **then**
    $T_{x,y}^{index} \leftarrow T_{x,y}^{groupindex,max}$ // Time bin information
    $N_{x,y}^{index} \leftarrow \sum N_{x,y}^{groupindex}$ // Reflection intensity information
    $Depth \Leftrightarrow \alpha T_{x,y}^{index}$
    $Reflection\ intensity \Leftrightarrow N_{x,y}^{index}$ // Time bin vs. Depth
  **end**
**end**

// Third Step: Wiener-Hopf Adaptive Filtering + deconvTV

$$H_{Depth}(f) = \frac{S_{y_{Depth}x}(f)}{S_{xx_{Depth}}(f) + \sigma^2_{v_{Depth}}} \qquad H_{Refl}(f) = \frac{S_{y_{Refl}x}(f)}{S_{xx_{Refl}}(f) + \sigma^2_{v_{Refl}}}$$

$\rightarrow \mathrm{L} = \mathtt{deconvTV}(P^* \mathcal{F}^{-1}\{H_{\mathrm{p}}(f)\})$

→ Global Morphological Constraints

// Fourth Step: Real-ESRGAN, Super resolution enhancement

First, the raw echo signal is converted into pixel space-arranged data, and the mask length is set according to the system characteristics to filter out the noise generated in the echo signal within the system. Second, matched filtering and extremely large group value estimation are used to obtain the depth and reflectivity information of the acquired target scene. In Algorithm1, $s^*(-t)$ denotes that the impulse response of the matched filter is the time inversion and conjugate of the transmitted impulse signal; $y(t)$ denotes the output of the matched filter; $r(t)$ is the received echo signal; $T_{x,y}^{index}$ and $N_{x,y}^{index}$ denote the time value of the current pixel and the number of the photons in the group; $T_{x,y}^{groupindex,max}$ and

$N_{x,y}^{groupindex}$ denote the time of the bin with the largest number of the photons in the group and the number of the photons in each bin in the group, respectively; $\alpha$ is the time-distance conversion coefficient; and Depth and Reflection intensity are the preliminary reconstructed depth and reflection intensity maps of single-photon lidar, respectively. After that, the Wiener–Hopf filter [55,56] with improved decisionTV [57] smoothing constraints is used to remove anomalies while retaining the edge information. $H_{\mathrm{Depth}}(f)$ and $H_{\mathrm{Refl}}(f)$ denote the frequency response of the Wiener filter for the Depth and Reflection intensity signals, respectively; $S_{y_{\mathrm{Depth}}x}(f)$ and $S_{y_{\mathrm{Refl}}x}(f)$ denote the frequency response of the input Depth and Reflection intensity signals with respect to the desired Depth and Reflection intensity signals, respectively; $\sigma^2_{v_{\mathrm{Depth}}}$, $\sigma^2_{v_{\mathrm{Refl}}}$ denote the noise variance of the Depth and Reflection intensity signals, respectively; $P$ and L refer to the Depth and Reflection intensity signals before and after processing, respectively; and $\mathcal{F}^{-1}$ denotes the inverse Fourier transform. Finally, the clarity and visual quality of the images are enhanced by Enhanced Super-Resolution Generative Adversarial Networks (Real-ESRGAN). The reason for choosing this network is that it currently provides clarity enhancement functions that do not require a large amount of data to train for the time being and can maintain good results.

### 2.1. Data Preprocessing

The data acquired by the single-photon lidar are stacked in one dimension and need to be converted into a two-dimensional spatial arrangement based on the scanning method to make the data easier to process and understand. In addition, since the presence of large noise within the system interferes with target information extraction, data cleaning is used to remove the accumulation of noisy photons on the time axis due to the system. Second, all photon histograms are assembled to find the peak moments to obtain the approximate distance of the target scene for imaging display. The data preprocessing schematic of the SUARF is shown in Figure 2.

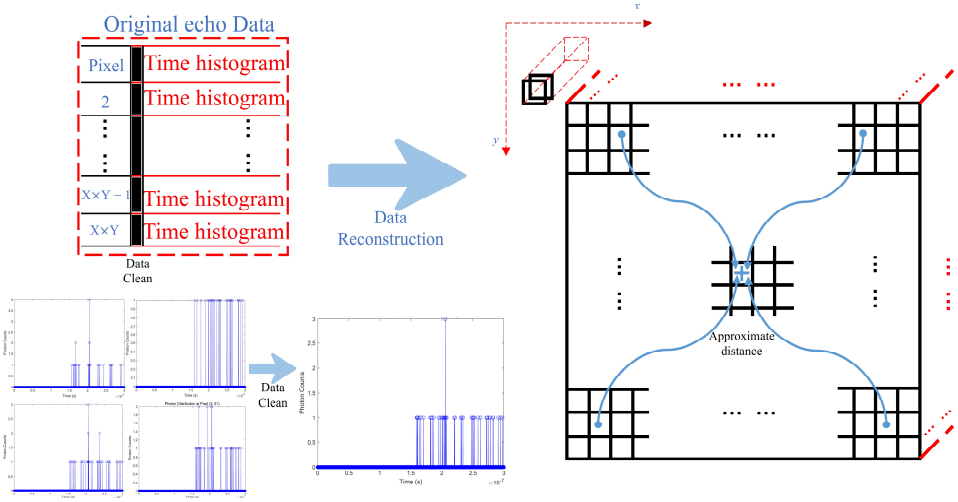


**Figure 2.** Schematic of data preprocessing of SUARF algorithm.

After setting the mask length BlindBin according to the empirical value of the system, the original data can be covered with this mask to shield specific elements, and the process can be described as Equation (1):

$$B_{\mathrm{masked}}(:,:,k) = \begin{cases} B(:,:,k) & \text{if } k > \mathrm{BlindBin} \\ 0 & \text{if } k \leq \mathrm{BlindBin} \end{cases} \quad (1)$$

$B_{\text{masked}}$ is the echo data after data reconstruction and cleaning, and $k$ is the index in the direction of the time axis. In Figure 2, it can be seen that after data preprocessing, the noise in the front part of the time axis has been filtered out. However, it should be noted that the length of BlindBin needs to be set according to the system; if it is arbitrarily set and set too large, it will cause the system to produce a large blind zone, and if it is set too small, the noise caused by the system will affect the determination of the time index and the number of photons.

### *2.2. Sequence Optimized Maximum Value Inference Filtering*

The signal of each pixel after data preprocessing is still time series information, which needs to be calculated by an inference algorithm to find the most compatible time and photon values. In this paper, we optimize previous research work [49] to obtain the information, and the processing schematic is shown in Figure 3.

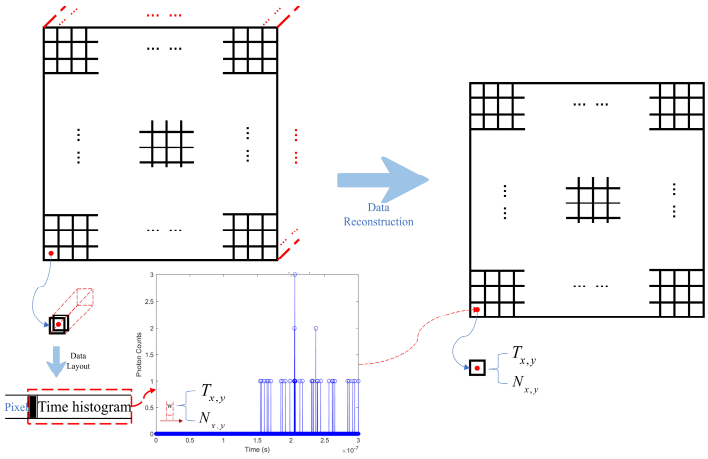


**Figure 3.** Schematic diagram of the sequence optimized maximum value inference filtering.

Assuming that the input signal is a superposition of the desired signal (target signal) and noise, where $s$(t) is the desired signal, $n$(t) is the noise, and the input signal $x$(t) can be denoted by Equation (2):

$$x(t) = s(t) + n(t) \tag{2}$$

The impulse response of the matched filter is the time reversal and conjugate complex of the desired signal $s(t)$ to make the filter most sensitive in detecting a particular signal. The designed filter and the output signal y(t) obtained after convolution with the input signal can be expressed, respectively, by Equations (3) and (4):

$$h(t) = s^*(-t) \tag{3}$$

$$y(t) = x(t) * h(t) = (s(t) + n(t)) * s^*(-t) \tag{4}$$

The amplitude of the output signal is maximized when the desired signal in the input signal exactly matches the impulse response of the filter, thus enabling the detection of the signal. And the convolution of noise n(t) with $s^*(-t)$ does not produce the same correlation peak as the desired signal $s(t)$, so the effect of noise in the output signal is suppressed, and the target signal in the original signal is more easily detected. Assuming that the size of the data volume after preprocessing and matched filtering is $X \times Y \times Z$, the first two dimensions denote the horizontal and vertical coordinates of the pixel, respectively, and the third dimension denotes the number of bin frames in the echo signal of each pixel, then

the number of bins and intra-bin photons in each pixel of the echo data are respectively expressed by Equations (5) and (6):

$$\left\{T_{x,y}^{1}, T_{x,y}^{2}, T_{x,y}^{3}, \ldots T_{x,y}^{Z}\right\} \tag{5}$$

$$\left\{N_{x,y}^{1}, N_{x,y}^{2}, N_{x,y}^{3}, \ldots N_{x,y}^{Z}\right\} \tag{6}$$

We select the width of the group (i.e., the length of the sliding window w. According to the experimental observation and the characteristics of the signal noise distribution, w = 5 bin can take into account the selection of the signal and avoid the selection of the noise peaks), and slide the group along the time axis with a step of 1 bin. Then we select the group with the highest number of photons in the group as the group where the target signal is located, then the bin and the number of photons in the bin of the group's echo data are numbered, respectively, by Equations (7) and (8); the time value and photon value of the pixel are calculated, respectively, by Equations (9) and (10):

$$\left\{T_{x,y}^{\phi,1}, T_{x,y}^{\phi,2}, T_{x,y}^{\phi,3}, \ldots T_{x,y}^{\phi,\mathrm{w}}\right\} \tag{7}$$

$$\left\{N_{x,y}^{\phi,1}, N_{x,y}^{\phi,2}, N_{x,y}^{\phi,3}, \ldots N_{x,y}^{\phi,\mathrm{w}}\right\} \tag{8}$$

$$T_{x,y} = \max\left\{T_{x,y}^{\phi,1}, T_{x,y}^{\phi,2}, T_{x,y}^{\phi,3}, \ldots T_{x,y}^{\phi,\mathrm{w}}\right\} \tag{9}$$

$$N_{x,y} = \sum\left\{N_{x,y}^{\phi,1}, N_{x,y}^{\phi,2}, N_{x,y}^{\phi,3}, \ldots N_{x,y}^{\phi,\mathrm{w}}\right\} \tag{10}$$

In the Equations (7)–(10), $T_{x,y}^{\phi,\mathrm{w}}$ and $N_{x,y}^{\phi,\mathrm{w}}$ denote the number of bin and bin photons in the $\phi$th group selected in the $(x, y)$ pixel. Considering that there are very few echo photons in the low illumination environment, the time index of the maximum number of photons and the sum of the number of photons in the group are used as the time value $T_{x,y}$ of the pixel, and the value of the photons $N_{x,y}$, respectively:

$$D_{x,y} = c \times T_{x,y}/2 = c \times \max\left\{T_{x,y}^{\phi,1}, T_{x,y}^{\phi,2}, T_{x,y}^{\phi,3}, \ldots T_{x,y}^{\phi,\mathrm{w}}\right\}/2 \tag{11}$$

Combined with the underwater speed of light $c$, the depth information for that pixel can be obtained by Equation (11). Repeating the operation (Equations (7)–(11)) for each pixel, the depth and reflectance information of the target scene can be preliminarily reconstructed

### *2.3. Collaborative Variation Strategy for Image Optimization*

Due to the complexity of light attenuation in the underwater environment, there is still some missing information and noise interference in the depth and reflectance map of the initial reconstruction. To eliminate this effect, we improve the idea of total variational smoothing constraints, add adaptive filtering and mixed morphological constraint structures to the deconvTV, and by dynamically adjusting the filtering parameters, we expect to suppress the abnormal pixels while better preserving the image edges and textures and protecting the naturalness and visual details of the image. The output processing flowchart of the collaborative variation strategy for image optimization is shown in Algorithm 2.

**Algorithm 2** Co-variation imaging strategy

**Function** Input Image (*fileP ath*)
**Define Blur and Regularization Parameters** {Create a blur kernel representing the average blur} {Set the regularization parameter balancing deblurring and Parameters}
$H \leftarrow$ create blur kernel(3)
$\mu \leftarrow 0.015$
**End of Define Blur and Regularizationnoise suppression**
**Filtering and regularization** {Apply the Wiener-Hopf filter to the Intput image} {Extract the channel data $I_c$ from the image $I$} {Simulate the blurred image $g$ by convolving $I_c$ with the blur kernel $H$}
$\text{OutputIm} = \text{Wiener} - \text{Hopf}\ (\text{InputIm})$
**for** each channel c in the image **do**
$I_c \leftarrow \text{extract\_channel}(I, c)$
$g \leftarrow I_c H$
$x^{(k+1)}$ {Refine the image $x^{(k+1)}$ using deconvolution}
apply deconvolution($x^{(k)}$, $H$, $\mu$)
**end for**
**End of Filtering and regularization**
**Post-Processing** {Combine the deconvolved channels to form the restored image $I_{\text{restored}}$}
$I_{\text{restored}} \leftarrow \text{merge\_channels}(x^{(k+1)})$ {Detect edges $E$ in the restored image using an edge detection method}
$E \leftarrow$ detect_edges(I_ restored) {Refine edge boundaries $E_{\text{closed}}$ using morphological closing}
$E_{\text{closed}} \leftarrow$ refine edges(E)
**End of Post-Processing**
**Morphological Reconstruction** Compute the distance map $D$ from the closed edges} {Reconstruct the im age $I_{\text{reconstructed}}$ based on the distance map $D$ and edges}
$D \leftarrow \text{compute distance map}(\text{E}_{\text{closed}})$
$I_{\text{reconstructed}} \leftarrow$ reconstructed_image($E_{\text{closed}}$,$D$)
**End of Morphological Reconstruction**
**Region Processing** {Label connected regions $L$ in the reconstructed image} {Find pixels in $P_k$ in region $k$} {Determine the most fre- quent value $v_k$ in region $k$} {Set all pixels in region $k$ to the most frequent value $v_k$}
$L,\ N \leftarrow \text{label\_regions}(I_{\text{reconstructed}})$
**for** each region $k$ from 1 to $N$ **do**
$P_k \leftarrow \text{find\_pixels}(L, k)$
$v_k \leftarrow \text{find\_mode}(I_{\text{restored}}(P_k))$
$I_{\text{restored}}(P_k) \leftarrow v_k$
**end for**
**End of Region Processing**
**EndFunction**

After obtaining the depth and reflectance 2D matrices of the target scene from the sequence optimized maximum value inference filtering, we use Wiener–Hopf adaptive filtering to adaptively adjust the filtering parameters with the help of the local statistical properties of the image, where the behavior of the filter varies in different regions of the image, thus removing anomalous pixel values while preserving the edges and details and providing clean pixel environments for smoothing constraints The filtered depth

image $D_{\text{Wiener}-\text{Hopf}}$ and the reflectance image $R_{\text{Wiener}-\text{Hopf}}$ can be obtained, respectively, by Equations (12) and (13):

$$D_{\text{Wiener}-\text{Hopf}}(i,j) = \frac{\sum_{k=-\infty}^{+\infty}\sum_{l=-\infty}^{+\infty} H(i-k,j-l)\cdot D_{\text{noisy}}(k,l)}{\sum_{k=-\infty}^{+\infty}\sum_{l=-\infty}^{+\infty} H(i-k,j-l)^2 + \frac{\sigma_{nD}^2}{\sigma_D^2(i,j)}} \tag{12}$$

$$R_{\text{Wiener}-\text{Hopf}}(i,j) = \frac{\sum_{k=-\infty}^{+\infty}\sum_{l=-\infty}^{+\infty} H(i-k,j-l)\cdot R_{\text{noisy}}(k,l)}{\sum_{k=-\infty}^{+\infty}\sum_{l=-\infty}^{+\infty} H(i-k,j-l)^2 + \frac{\sigma_{nR}^2}{\sigma_R^2(i,j)}} \tag{13}$$

In Equations (12) and (13), $D_{noisy}\ (i,j)$ and $R_{noisy}\ (i,j)$ are the depth map and the reflection intensity map pixel value at pixel (*i,j*), respectively. (*i,j*) and (*k,l*) are pixel indices in the image matrix, where (*i,j*) denotes the pixel position currently being processed and (*k,l*) denotes the position in the neighboring area covered by the filter. $H(i-k,j-l)$ is the impulse response of the filter (which can be calculated by Equation (14)), $\sigma_{nD}^2$, $\sigma_{nR}^2$ are the noise power, and $\sigma_D^2\ (i,j)$, $\sigma_R^2\ (i,j)$ are the local variance of the depth map and reflection intensity map at position (*i,j*), respectively:

$$H(e^{j\Omega}) = \frac{S_{xr}(e^{j\Omega})}{S_{xx}(e^{j\Omega}) + S_{nn}(e^{j\Omega})} \tag{14}$$

$S_{xr}\ (e^{j\Omega})$ , $S_{xx}\ (e^{j\Omega})$ and $S_{nn}\ (e^{j\Omega})$ are, respectively, the cross-power spectral density between the estimated signal and the desired response, the power spectral density of the signal, and the power spectral density of the noise from the pixel data.

Wiener–Hopf adaptive filtering can effectively suppress noise, but due to the low signal photon counts (average single-pixel photon counts $\not> 1$ in the reconstructed maps at times), it is inferred that too much variance of the filtered values leads to large uncertainty in the reconstruction of the image, and this uncertainty may lead to significant reconstruction errors. To reduce this uncertainty, the smoothing constraint maintains the edge information by minimizing the sum of the absolute values of the image gradients while suppressing the noise, while further mixed morphological reconstruction is employed to enhance the details by highlighting the edges and textures in the image in order to improve the accuracy of the image reconstruction and to enhance the visual effect. For the acquired depth image $D_{\text{Wiener}-\text{Hopf}}$ and reflectance image $R_{\text{Wiener}-\text{Hopf}}$, the deconvTV algorithm is used to stabilize the image reconstruction results. Considering the underwater application scenario of single-photon lidar, we improve the idea of morphological constraints by extracting the global features of the image and fusing them with the local features, and improving the image quality through the assisting deconvTV algorithm by erosion, expansion, and open/close operations, etc. This module (TV-Morphological Restoration Algorithm, TVMR) can be described by the following equation:

$$\text{FinalImg} = \text{MorphologicalReconstruct}(\text{Edges}(\text{deconvTV}(\text{Img}, \text{H}, \text{Opts}))) \tag{15}$$

Img is the pending $D_{\text{Wiener}-\text{Hopf}}$ and $R_{\text{Wiener}-\text{Hopf}}$, deconvTV (Img,*H*,Opts) denotes the processing of the image using full variational deconvolution, where *H* is the point spread function (PSF) and Opts are the algorithmic options (containing regularization parameter $\mu$, initial penalty parameter *rho_r*, maximum number of iterations *max_itr*, regularization parameter *beta* for weight TV paradigm, update constant *gamma*, tolerance *tol*, etc.). Edges denotes Canny edge detection (enhanced edge display) of the image and

Morphological Reconstruct denotes improved morphological reconstruction of the image. Since the system uses Gaussian beams, its PSF can be expressed as (16):

$$\mathrm{PSF}(x,y) = \frac{1}{\sqrt{2\pi\sigma^2}} e^{-\frac{x^2+y^2}{2\sigma^2}} \tag{16}$$

PSF($x$,$y$) denotes the value of the point spread function at position ($x$,$y$) and $\sigma$ is the standard deviation of the Gaussian beam, then the deconvTV algorithm can be calculated as Equation (17):

$$\begin{cases} D_{\mathrm{deconvTV}} = \mathrm{argmin}_D \left\{ \lambda \left\| D - D_{\mathrm{Wiener-Hopf}} \right\|_2^2 + \tau \|\nabla D\|_1 \right\} \\ R_{\mathrm{deconvTV}} = \mathrm{argmin}_R \left\{ \lambda \left\| R - R_{\mathrm{Wiener-Hopf}} \right\|_2^2 + \tau \|\nabla R\|_1 \right\} \end{cases} \tag{17}$$

In Equation (17), $D_{\mathrm{deconvTV}}$ and $R_{\mathrm{deconvTV}}$ are the depth image and reflection intensity image after the constraints of the deconvTV algorithm. $D$ and $R$ are the variables in the optimization problem, $\lambda$ is the regularization parameter of the data fidelity term, $\tau$ is the regularization parameter of the total variation term, and $\nabla$ denotes the gradient operator. Further, the mixed morphological reconstruction method with the fusion of global and local features is used, and the processing sequence is (1) edge detection and morphological closure operation, (2) distance transformation and morphological reconstruction, and (3) connected region processing and enhancement. Since the processing steps of depth image and reflection intensity image are the same, $D_{\mathrm{deconvTV}}$ and $R_{\mathrm{deconvTV}}$ are standardized to be described by $I_{\mathrm{restored}}$ instead. The edge detection and mixed morphological closure operations are as Equation (18):

$$E_{\mathrm{closed}} = \mathrm{close}(\mathrm{C}(I_{\mathrm{restored}}), \mathrm{S}(N)) \tag{18}$$

In Equation (18), $\mathrm{C}(I_{\mathrm{restored}})$ denotes the extraction of edges for the image $I_{\mathrm{restored}}$, 'close' denotes the morphological closure operation, and $\mathrm{S}(N)$ is used to define the neighborhood of pixels in the image. Then the distance transformation is performed based on the edge map after the closed operation as Equation (19):

$$I_{\mathrm{Reconstructed}} = \mathrm{Reconstruct}(E_{\mathrm{closed}}, \frac{\mathrm{W}(\sim E_{\mathrm{closed}})}{\max(\mathrm{W}(\sim E_{\mathrm{closed}}))}) \tag{19}$$

In Equation (19), W(~E closed) computes the distance transform of the complement of the edge map after the closure operation, max(·) denotes the normalization operation, and 'Reconstruct' denotes the morphological reconstruction based on the distance transform and the edge map. Finally, the connected regions in the reconstructed image are processed to enhance the visual contrast effect. In the process of enhancing the imaging results, we adjust the specific values of the two parameters and observe their imaging results. We found that when regularization parameter $\tau$ is set to about 0.015 and morphological constraint size parameter *se* is set to about 10, the image enhancement effect is better, and the details are saved more completely. Of course, this may need to be adjusted slightly in different LiDAR systems.

$$I_{\mathrm{final}} = \widehat{\mathrm{Sharpen}}\left( \bigcup_{k=1}^{\mathrm{num}} (\mathrm{LabelImg} == \mathrm{k} \Rightarrow \mathrm{mode}(\mathrm{I}_{\mathrm{Reconstructed}}(\mathrm{LabeledImg} == \mathrm{k}))) \right) \tag{20}$$

In Equation (20), 'LabelImg==k' denotes the connected region labeled as k, mode(·) denotes all pixel values in the statistical region, ∪ denotes all connected regions, and $\widehat{\mathrm{Sharpen}}(\cdot)$ denotes that while the traditional image processing techniques are mainly used,

Real-ESRGAN [58] can be used as an auxiliary tool, and its pre-trained model can be directly used for image clarity, which further improves image resolution and visual effect.

## 3. Construction of Test Device and Analysis of Land Imaging

We constructed a single-photon lidar system to verify the algorithm imaging effect. Considering the underwater application scenarios of single-photon lidar, the main reason we chose the scanning imaging single-photon lidar system instead of gaze imaging is its high sensitivity and high spatial resolution. The scanning system is able to adapt to different detection needs by adjusting the scanning mode and speed, which is especially important for the changing underwater environment. In addition, single-photon lidar technology, especially single-photon avalanche diode (SPAD)-based systems, offers unique technological advantages in capturing weak signals and high-precision imaging due to its high temporal resolution, high sensitivity, and ease of integration. These advantages make scanning single-photon lidar systems more effective in underwater target detection and imaging.

The main components of the system are a transmitter module, a receiver module, an optical system module, a scanning imaging module, a time-dependent single-photon counter, and a signal control module. The schematic diagram of the system is shown in Figure 4.

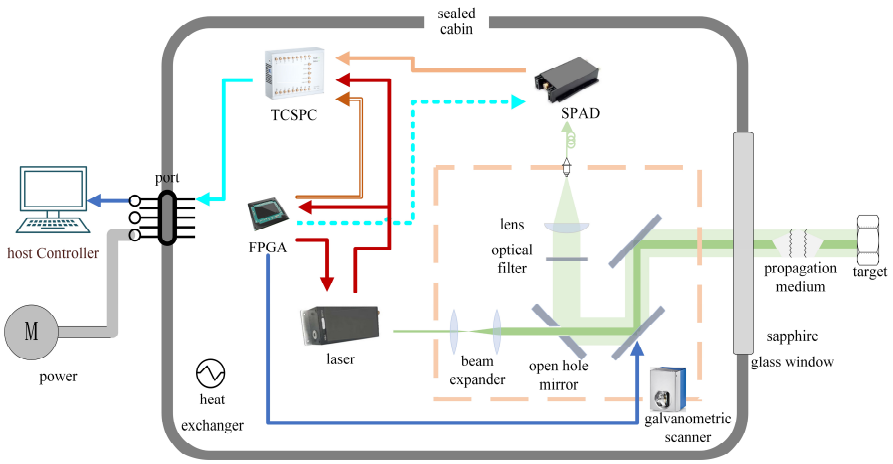


**Figure 4.** Schematic diagram of the system principle.

The transmitting module uses a 532 nm wavelength solid-state laser as the light source, which is a common green laser suitable for underwater environments, with high stability and reliability. The laser operates in a pulsed mode with a repetition rate of 1–5 kHz, allowing for high-resolution imaging by emitting short bursts of light at regular intervals. The average power of 175 mW and single pulse energy of 35 μJ ensure that the laser can provide sufficient energy for long-distance detection while maintaining the high quality of the beam. The receiving module collects the photons reflected from the target using a flat-convex lens with a focal length of 100 mm and a diameter of 2 inches. This lens focuses the incoming photons onto a multimode fiber with a core diameter of 105 μm and a numerical aperture of 0.22. The fiber then couples the photons to a single-photon detector. A bandpass filter with a central wavelength of 532 nm and a transmittance of 53.58% is used to filter out non-target wavelength light, ensuring that only 532 nm wavelength photons reach the detector. The system adopts a coaxial transceiver combined optical path design, using a 45° open-hole mirror as a transceiver switch. This mirror allows the laser to be transmitted and received in the same optical path, greatly improving the compactness and efficiency of the system.

The scanning imaging module uses a two-axis galvanometer for two-dimensional beam scanning with an optical deflection angle of ±22.5° and an optical resolution of 12 μrad. The galvanometer works by using electromagnetic coils to rotate mirrors, which in turn deflect the laser beam to scan the target area. The time-dependent single-photon counter (TCSPC) module measures the arrival time of each detected photon by recording the time interval between the emission of the laser pulse and the detection of the reflected photon. It converts the electrical signal from the detector into digital time-stamped data, allowing the system to determine the total flight time of the photon and calculate the distance to the target. The signal control module coordinates the gating mode of the single-photon detector, generates the reference time signal required by the TCSPC, and controls the pulse output of the laser. It ensures the synchronization of all components by managing the timing and control signals, thus ensuring the accuracy and reliability of the data.

In the workflow of our system, the 532 nm solid-state laser first emits a pulsed laser. When the photodetector detects the pulsed laser, it outputs an electrical pulse synchronization signal, which is collected by the time-dependent photon counting module and starts timing. The outgoing pulsed laser increases the beam diameter and decreases the divergence angle by shaping the optical path, and changes the direction by the two-axis galvanometer to reach the target point. When the photon returns to the system in the form of diffuse reflection from the target, the propagation direction is changed again through the two-axis galvanometer, and then the incoming echo receiving module is coupled. The SPAD detector generates an electrical pulse signal immediately after receiving the echo photon, and the TCSPC module subtracts the time generated by the electrical signal and the time of the synchronization signal when the pulse laser emits, so as to obtain the total flight time of the outgoing photon; then, we can calculate the numerical distance of the target point. The input and output signals dependent on each module in the system are uniformly managed by the signal control module. The data of the time-dependent photon counting module flows through the host computer and is directly read by the software algorithm for imaging and image enhancement optimization. We first verified the imaging performance of the system in a land trial. The two targets designed in previous work were used to verify the imaging effect, the targets are target A and target B, which are shown in Figure 5.

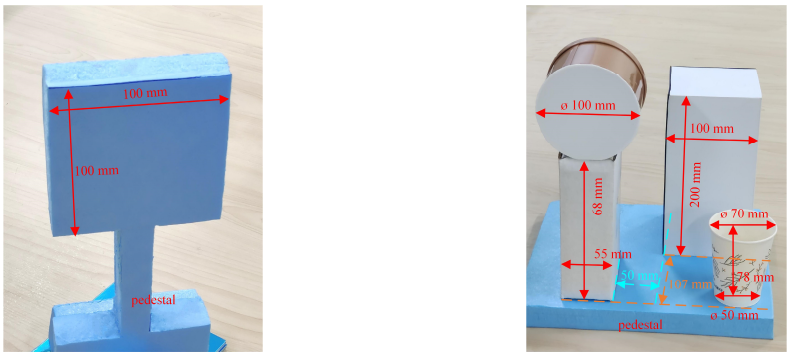


Target A Target B

**Figure 5.** Schematic diagram of the target.

In Figure 5, target A is a regular 10 × 10 cm square, and in target B there are circles, rectangles, etc., distributed in different depth areas. It should be noted that, in order to ensure the randomness and fairness of the test, the data of two kinds of targets were randomly selected from the results of multiple data acquisition for imaging analysis. By varying the detection distance, the number of emitted pulses, and the intensity of the

external light intensity, respectively, the imaging results of the SUARF algorithm are as Figures 6–11.

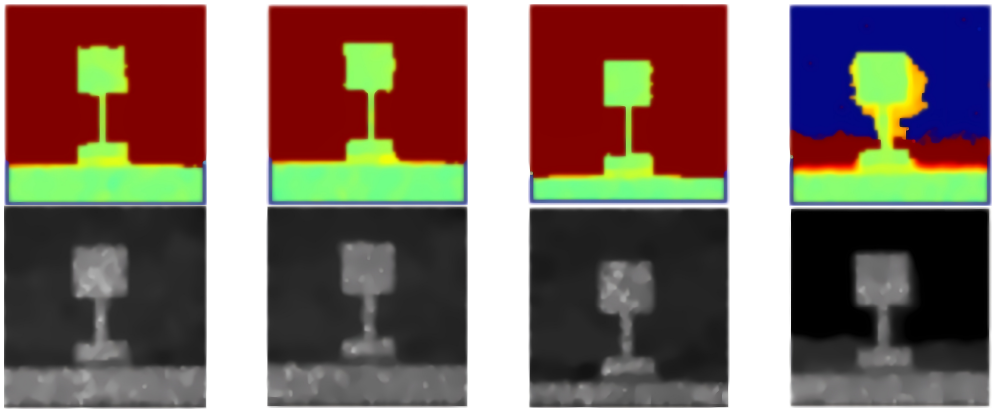

**Figure 6.** The reconstruction results of the SUARF algorithm on target A when the external light intensity is 0.1/2374/5450/44355 Lux.

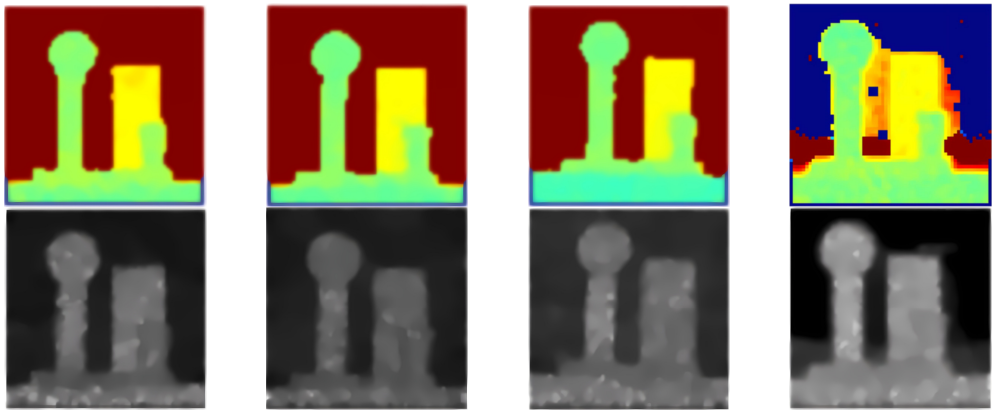

**Figure 7.** The reconstruction results of the SUARF algorithm on target B when the external light intensity is 0.1/1102/16172/44364 Lux.

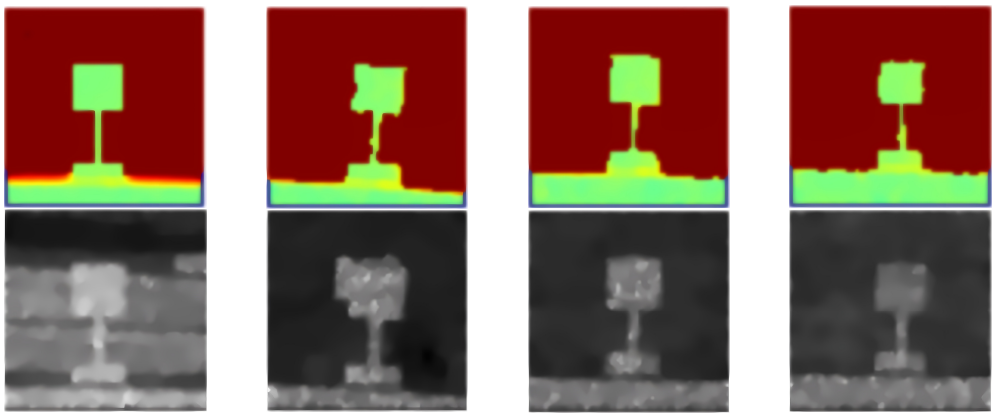

**Figure 8.** The reconstruction results of the SUARF algorithm for target A when the imaging distance is 10/25/40/55 m.

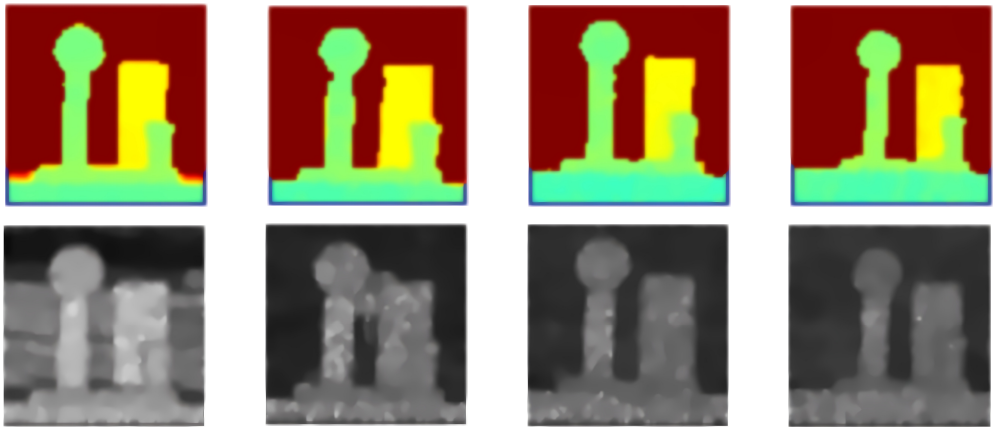

**Figure 9.** The reconstruction results of the SUARF algorithm for target B when the imaging distance is 10/25/40/55 m.

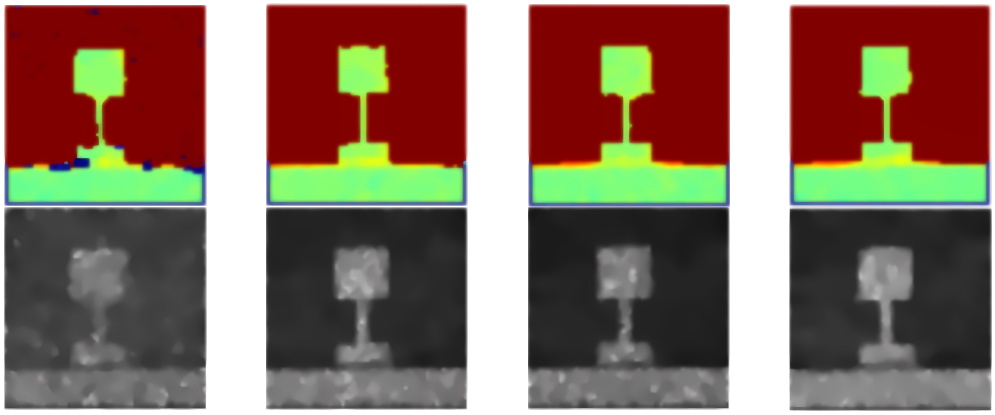

**Figure 10.** The reconstruction results of the SUARF algorithm for target A when the number of single pixel pulses is 5/50/100/500.

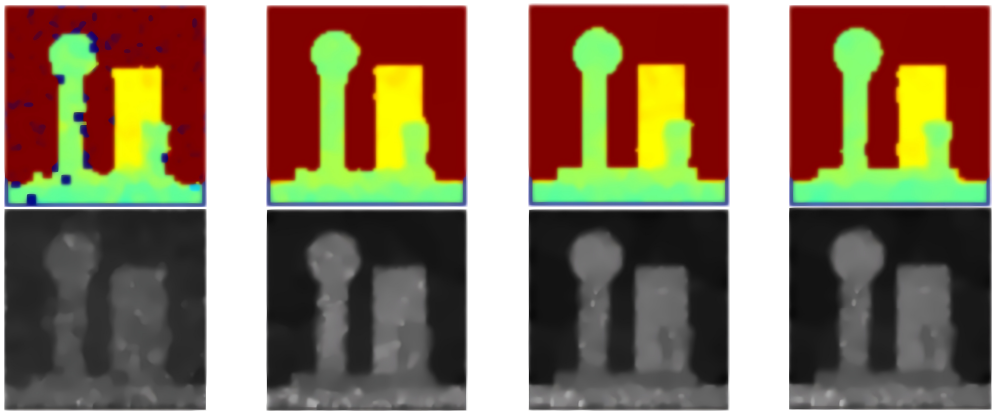

**Figure 11.** The reconstruction results of the SUARF algorithm for target B when the number of single pixel pulses is 5/50/100/500.

In Figures 6 and 7, the system is tested at a distance of about 40 m, the number of pixels collected is 64 × 64, and the number of single-pixel pulses is 50. From the reconstruction results, it can be seen that the SUARF algorithm maintains a better imaging effect with the enhancement of the external light intensity interference. In Figures 8 and 9, the number of pixels collected by the system is 64 × 64, and the number of single-pixel pulses is 50. From the reconstruction results, it can be seen that the SUARF algorithm maintains a better imaging effect with the increase of the imaging distance (the number of attenuation lengths, AL). In Figures 10 and 11, the number of pixels acquired by the system is 64 × 64, and it can

be seen that the SUARF algorithm still maintains a good imaging effect under the condition of low pulse number. Therefore, the SUARF algorithm is robust and can be tried for underwater imaging. The mainstream imaging algorithms for scanning single-photon lidar systems are first-photon, first-photon group algorithm, peak algorithm, STMF algorithm, etc. The STMF algorithm has strong anti-noise and convenience compared with the first photon, the first photon group, and the peak algorithm, etc., and has obvious advantages in imaging ability under general imaging conditions. Therefore, this paper mainly analyzed the performance of the SUARF algorithm reported here by comparing the STMF algorithm.

## 4. Underwater Test and Result Analysis

In underwater environments, conventional imaging techniques face many challenges due to the strong absorption and scattering of light, which make it extremely difficult to acquire high-contrast and high-resolution images. With its extremely high detection sensitivity, single-photon lidar technology is able to capture weak echo signals in this low-light and high-noise environment, thus realizing precise detection and imaging of underwater targets. Therefore, the practical application of single-photon lidar underwater can not only significantly improve the quality and depth resolution of underwater imaging, but also extend its application potential in many fields such as marine exploration, underwater archaeology, environmental monitoring, and underwater navigation, which is of great significance for both scientific research and industrial applications. In order to verify the environmental adaptability of the SUARF algorithm, we built four underwater environments for scene reconstruction experiments, namely, a swimming pool, pipeline (a drain placed horizontally), and the actual waters off the coast of China. According to the performance of the system, the target deployment distance from the lidar is about 5~6 AL.

### *4.1. Comparative Analysis of the Reconstruction Effect of Each Algorithm*

#### 4.1.1. Pool Reconstruction Tests

The underwater experiments were first carried out in a pool in the laboratory. The available dimensions of the pool are about 12 × 13 × 6 $m^3$, and the lidar and the target were placed at the two ends of the pool, respectively (Figure 12a). Due to the extremely poor visibility, the underwater visible light camera cannot shoot the target at all at the location of the lidar, such as Figure 12b.

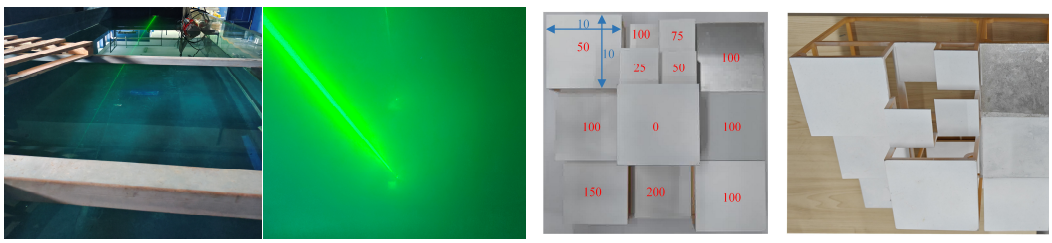


(**a**) (**b**) (**c**) (**d**)

**Figure 12.** Schematic diagram of pool experiment and test target.

The target used for the pool was a multiplanar target (Figure 12c,d), with the highest square plane as the datum plane. The target information of the multi-depth target contains 12 planes in total at depths of 0/25/50/75/100 (three types of reflectivity)/150/200 cm. The pool style is shown in (a) and the water is rather turbid, as shown in (b), and the underwater camera can't capture the target and LIDAR even at very close range. The results of the algorithms are shown in Figures 13 and 14.

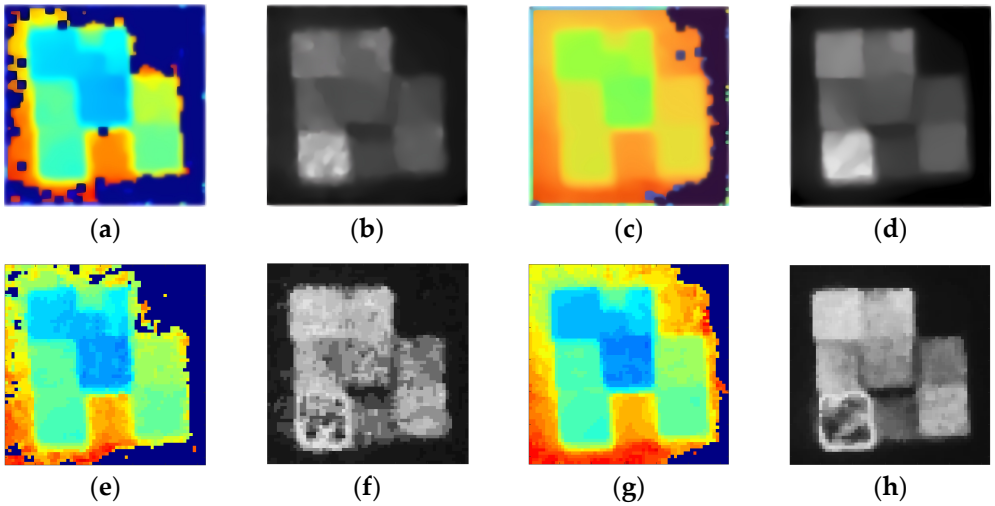


**Figure 13.** Results of pool target reconstruction for SUARF and STMF algorithms.

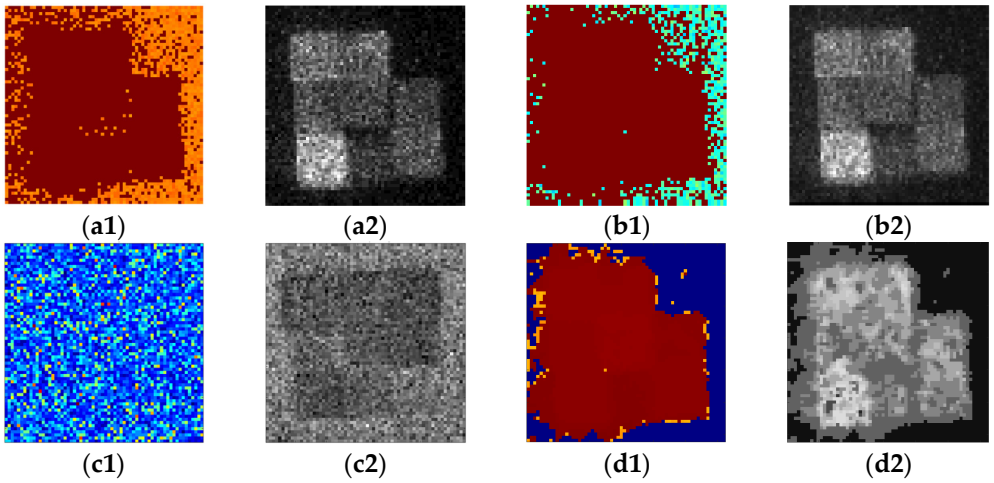


**Figure 14.** Results of pool target reconstruction for peak (**a1**,**a2**), cross-correlation (**b1**,**b2**), first photon (**c1**,**c2**), and first photon group (**d1**,**d2**) algorithms.

Figure 13a,b shows the results of the SUARF algorithm, and Figure 13e,f the results of the STMF algorithm. Figure 13a,b,e,f shows the imaging results at a pulse number of 50, Figure 13c,d,g,h the imaging results at a pulse number of 500. Figure 14a–d depicts the depth map (1) and reflection intensity map (2) obtained at the pulse number of 50 by using the peak, inter-correlation, first-photon, and first-photon group algorithms, respectively. It can be seen that the SUARF algorithm has the ability to repair anomalies on the basis of strong information extraction capability, and the depth resolution reaches 2.5 cm (the limit of the depth resolution of the device is 3 cm).

#### 4.1.2. Quantitative Evaluation Criteria

Structural similarity index (SSIM) and root mean square error (RMSE) as well as subjective judgment are used to comprehensively evaluate the effectiveness, and the comparative reference is the adopted image at 500 pulses in Figure 15. Visible light struggles to capture clear high-resolution images in the complex experimental water environment, while longer observation times with time-counting single-photon LiDAR generally improve reconstruction quality, as confirmed in the paper's Section 3 air experiment. We chose 500 pulses as the evaluation index, because beyond this point additional pulses in our underwater system did not significantly enhance imaging but increased processing time. In practice, balancing the number of emitted pulses with observation effects is crucial to optimize

imaging performance and efficiency. The reconstruction results for peak, inter-correlation, first-photon, first-photon group, STMF, and SUARF algorithms are shown in Tables 1 and 2.

**Table 1.** The depth reconstruction results of evaluation index values of each algorithm.

| Index | Peak | Cross-Correlation | First Photon | First Photon Group | STMF | SUARF |
|---|---|---|---|---|---|---|
| SSIM | 0.373 | 0.376 | 0.293 | 0.512 | 0.723 | 0.828 |
| RMSE | 134.451 | 127.358 | 100.836 | 111.149 | 68.431 | 29.500 |

**Table 2.** The reflection intensity reconstruction results of evaluation index values of each algorithm.

| Index | Peak | Cross-Correlation | First Photon | First Photon Group | STMF | SUARF |
|---|---|---|---|---|---|---|
| SSIM | 0.590 | 0.630 | 0.408 | 0.568 | 0.563 | 0.833 |
| RMSE | 31.015 | 28.51 | 80.833 | 55.400 | 58.354 | 17.125 |

SSIM is an evaluation index of the similarity of two images, proposed by the Laboratory for Image and Video Engineering at the University of Texas at Austin [59]. It takes into account the brightness, contrast, and structural information of the images. Unlike traditional error metrics (e.g., MSE), SSIM is more in line with the perceptual properties of the human visual system. SSIM has a value between 0 and 1, where 1 means that the two images are exactly the same. The computation of SSIM involves localized windows of an image and assesses the similarity between the images by comparing the statistical properties within these windows. It not only takes into account the pixel-level differences but also the overall structural information of the image and is therefore widely used in image quality evaluation. RMSE [60] is a measure of the difference between predicted and actual values. It is the square root of the mean square error (MSE), which calculates the average of the squares of the differences between the predicted and actual values. It provides a visual measure of the magnitude of the error, with smaller values indicating that the model's predictions are closer to the actual values. RMSE is very sensitive to outliers, and therefore its value increases significantly when there is a large bias in the data, reflecting model variability in these points of variability. These two metrics provide a quantitative assessment of data similarity and prediction accuracy from different perspectives and are very important tools in the field of image processing. SSIM focuses on visual quality and can detect visual distortion and structural changes of images, while RMSE, on the other hand, focuses on the size of the error and can quantify the difference between the predicted value and the actual value. The combination of SSIM and RMSE can comprehensively reflect the visual similarity of images and the size of prediction error, help better understand the overall performance of the imaging effect, and provide more accurate and reliable evaluation results for the optimization and improvement of image processing algorithms. In Tables 1 and 2, the SUARF algorithm reported in this paper has the largest SSIM value and the smallest RMSE value. Compared with the STMF imaging algorithm, with the best performance at present, the imaging results of the SUARF algorithm proposed in this paper increase the SSIM and RMSE of the depth and reflection intensity map by 15%, 57% and 48%, 71%, respectively. It can discriminate 2.5cm@5-6AL in the imaging results, and it can discriminate targets with different reflectance.

Based on the subjective judgment results of 20 randomly selected groups (five people in each group), without observing the target in advance, more than 95% of the personnel think that the reconstruction results of the SUARF algorithm are the most intuitive, and there are very few anomalies. Since both depth and reflection intensity reconstruction are crucial for understanding the target, and RMSE and SSIM are two indicators for comprehensively

evaluating the reconstruction effect, we defined a comprehensive indicator to evaluate the reconstruction results of the algorithm, which is shown in Equation (21):

$$R_{\mathrm{T}} = \omega_1 \times \frac{1}{RMSE_{\mathrm{D}}} + \omega_2 \times \frac{1}{SSIM_{\mathrm{D}}} + \omega_3 \times \frac{1}{RMSE_{\mathrm{R}}} + \omega_4 \times \frac{1}{RMSE_{\mathrm{R}}} \tag{21}$$

In Equation (21), $RMSE_{\mathrm{D}}$, $SSIM_{\mathrm{D}}$, $RMSE_{\mathrm{R}}$, $SSIM_{\mathrm{D}}$ are the evaluation index values of the depth map and reflection intensity map, respectively, and $\omega_1$, $\omega_2$, $\omega_3$, $\omega_4$ are the coefficients of the index values, which can be calculated as Equation (22):

$$\begin{cases} \omega_1 = \frac{1/RMSE_{\mathrm{D}}}{1/RMSE_{\mathrm{D}}+SSIM_{\mathrm{D}}+1/RMSE_{\mathrm{R}}+SSIM_{\mathrm{R}}} \\ \omega_2 = \frac{SSIM_{\mathrm{D}}}{1/RMSE_{\mathrm{D}}+SSIM_{\mathrm{D}}+1/RMSE_{\mathrm{R}}+SSIM_{\mathrm{R}}} \\ \omega_3 = \frac{1/RMSE_{\mathrm{R}}}{1/RMSE_{\mathrm{D}}+SSIM_{\mathrm{D}}+1/RMSE_{\mathrm{R}}+SSIM_{\mathrm{R}}} \\ \omega_4 = \frac{SSIM_{\mathrm{R}}}{1/RMSE_{\mathrm{D}}+SSIM_{\mathrm{D}}+1/RMSE_{\mathrm{R}}+SSIM_{\mathrm{R}}} \end{cases} \tag{22}$$

The value interval of $R_{\mathrm{T}}$ is [0, 1], and the closer the value is to 1, the better the comprehensive reconstruction effect of the algorithm. Through the $R_{\mathrm{T}}$ evaluation index, we can conduct a comprehensive evaluation of the RMSE and SSIM evaluation values of the depth and reflection intensity of the algorithm. The value of $R_{\mathrm{T}}$ for each of the above algorithms is calculated in Table 3.

**Table 3.** Evaluation metrics for each algorithm $R_{\mathrm{T}}$ values.

| Index | Peak | Cross-Correlation | First Photon | First Photon Group | STMF | SUARF |
|---|---|---|---|---|---|---|
| $R_{\mathrm{T}}$ | 0.487 | 0.514 | 0.349 | 0.529 | 0.638 | 0.789 |

As can be seen from Table 3, $R_{\mathrm{T}}$ is increased by 24%. This index comprehensively reflects that the depth and reflectivity imaging results of the SUARF algorithm have been greatly improved compared with the latest algorithms. Combining the results of SSIM, RMSE, $R_{\mathrm{T}}$, and the subjective judgment of the randomly selected persons, the SUARF algorithm reported in this paper is more effective in reconstructing the target scene.

In addition, in order to further verify the lateral resolution effect of the SUARF algorithm, a hollow target plate (Figure 15) was used, with a lateral resolution of 5 mm at the smallest point. The reconstruction results of the algorithm are shown in Figure 16.


**Figure 15.** Hollow target board and underwater visible light camera close shot.

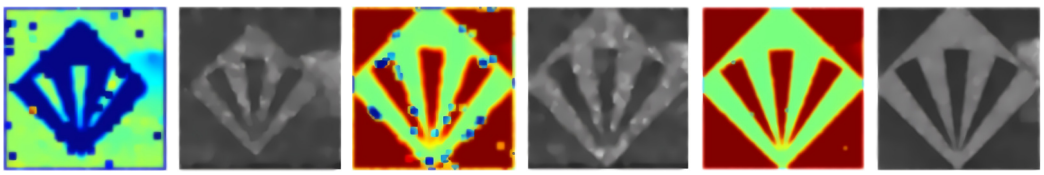


**Figure 16.** Imaging results of the SUARF target reconstruction algorithm for the hollow target plate. (**a**) Depth map, 32 pixels, 10 pulses. (**b**) Reflection intensity map, 32 pixels, 10 pulses. (**c**) Depth map, 64 pixels, 10 pulses. (**d**) Reflection intensity map, 64 pixels, 10 pulses. (**e**) Depth map, 128 pixels, 20 pulses. (**f**) Reflection intensity map, 128 pixels, 20 pulses.

As can be seen from the reconstruction results in Figure 16, the 32-pixels-10-pulses imaging results can already show the overall shape of the target plate, and the zone boundary can be distinguished. The target details for 128-pixels-20-pulses imaging results are fully revealed with a minimum resolution of about 5 mm.

### *4.2. Imaging Test of SUARF Algorithm in Different Environmental Waters*

The water environment is complex and changeable. In order to test whether the SUARF algorithm can be adapted to different waters for imaging, we also conducted tests in the pipeline, swimming pool, and actual water off the coast of China. The target placement distance from the lidar is about 5–6 AL. Affected by the space size of the experimental environment and the target placement sinking and floating, the target used in different environments is different. The test layout is as Figure 17 and the test target is shown in Figures 18–20.

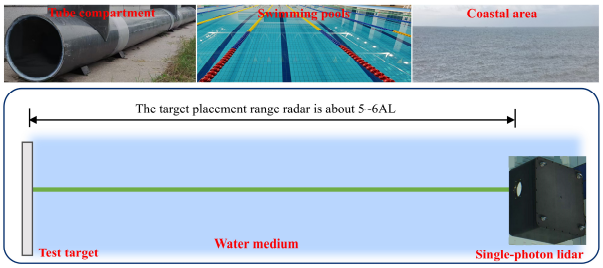


**Figure 17.** Experimental layout of SUARF target reconstruction algorithm in different waters.

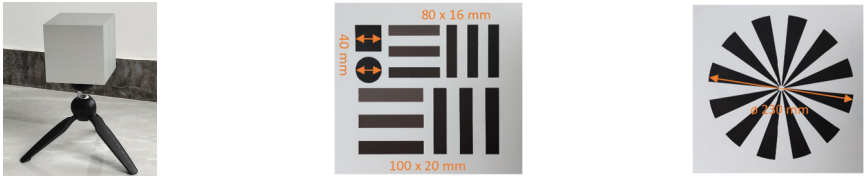


(**a**) (**b**) (**c**)

**Figure 18.** Targets used in pipeline test. (**a**) Metal cube. (**b**) Band target A. (**c**) Spoke-type target.

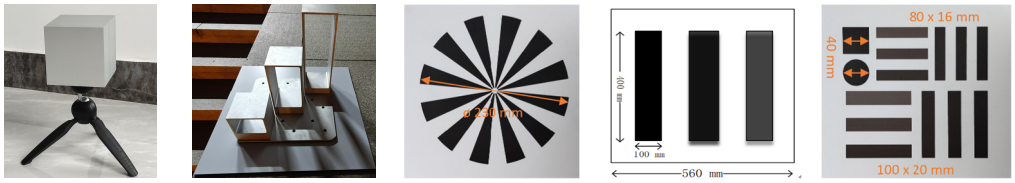


(**a**) (**b**) (**c**) (**d**) (**e**)

**Figure 19.** Targets used in swimming pool test. (**a**) Metal cube. (**b**) Diagonal ladder distribution of metal blocks. (**c**) Spoke-type target. (**d**) Band target B. (**e**) Band target A.

(**a**) (**b**)

**Figure 20.** Targets used in the actual water off the coast of China test. (**a**) Metal cube. (**b**) Spoke-type target.

In different water environments, we selected different target combinations to comprehensively evaluate the performance of the SUARF algorithm. In the pipeline, we used a metal cube, a band target A, and a spoke-type target to verify basic imaging capabilities. In

the swimming pool, a diagonal ladder distribution of metal blocks and a band target B were added to test the imaging effect of the algorithm on complex structures and different material targets. In the actual water area in winter, faced with the problems of water complexity, biodiversity, dynamic changes in the environment, artificial obstacles, and insufficient performance of hardware equipment, we chose a metal cube and a spoke-type target to test the performance; this can reduce the complexity of the test and verify the imaging resolution capability. In Figure 18, the metal cube has a volume of 10 × 10 × 10 cm. Band target A contains 10 × 2 cm and 8 × 1.6 cm bands with a 20% increase in color contrast from the top to the bottom, as well as squares and circles with a side length and diameter of 4 cm. The spoke-type target was 2.3 cm in diameter and contained 12 black spokes and 12 white spokes. Band target B and Diagonal ladder distribution of metal blocks were used as substitutes in the swimming pool, which contains three 40 × 10 cm rectangular bands with a contrast difference of 20–30% from left to right, and the stepped metal block contains three height difference of 10 cm rectangles (the shapes above are all 10 × 10 cm squares), respectively. The situation that needs further clarification is that, affected by the waves generated by underwater activities, the target will produce rapid jitter, which is not conducive to the deployment and observation of targets used in relatively controlled underwater environments such as laboratory pools and swimming pools in actual waters. Therefore, only the more challenging spokes target was used as a representative to test in the actual water. In addition, our goal was to test the adaptability and robustness of the SUARF in several underwater environments, rather than just pursuing the limits of the indexes. The limits of the indexes are closely related to both the hardware system and the algorithm. In the actual water test, we paid more attention to the performance of the algorithm in different environmental conditions, and how to optimize the algorithm to adapt to various complex situations. Therefore, the main purpose of the underwater single-photon lidar test machine built in this report is to cooperate with the algorithm test and verify the performance and effect of the algorithm in the real underwater environment. Therefore, in this case, the use of low-resolution targets is sufficient to meet the needs of testing the adaptability of the algorithm. Although high-precision targets can provide higher accuracy, such high accuracy is not necessary in real-water testing and will increase the complexity and cost of system testing. The reconstruction results in the pipeline are shown below.

In Figure 21, (a) is the depth map of the metal cube, (b) is the reflectance intensity map of the metal cube, (c) is the depth map of the band target A, (d) is the reflectance intensity map of the band target A, (e) is the depth map of the spoke-type target, and (f) is the reflectance intensity map of the spoke-type target. The first line (a1–f1)shows the imaging results using the first photon group algorithm, the second line (a2–f2) showsthe imaging results using the STMF imaging algorithm, and the third line (a3–f3) showsthe imaging results using the SUARF imaging algorithm proposed in this paper. According to the imaging results, for the simple geometry metal cube (a) and (b), the three algorithms can carry out relatively high-quality imaging. However, when the first photon group algorithm is used for imaging under different target needs, different environments, and different single-photon LiDAR systems, the imaging photon threshold needs to be adjusted from time to time. When the threshold is not chosen properly, imaging is not effective, and the poor imaging results are displayed in Figure 22.

In Figure 22, (a4) is the depth map of the metal cube, (b4) is the reflectance intensity map of the metal cube, (c4) is the depth map of the band target A, (d4) is the reflectance intensity map of the band target A, (e4) is the depth map of the spoke-type target, and (f4) is the reflectance intensity map of the spoke-type target. In addition, the first photon group algorithm lacks more information on the imaging edge of simple geometry; there

are more abnormal pixel values, and the imaging effect is not good for the objects (c4), (d4), (e4), and (f4) with higher horizontal resolution. Compared with the first photon group algorithm, the STMF algorithm has a stronger information ex-traction ability, but the boundary retention ability and pixel outlier removal ability need to be further enhanced. The SUARF algorithm proposed in this paper has stronger detail display and outlier processing capabilities. In order to further confirm the imaging ad-vantages of the SUARF algorithm, we conducted comparative tests on the imaging results of the swimming pool, simultaneously, and the results are as Figures 23–25.

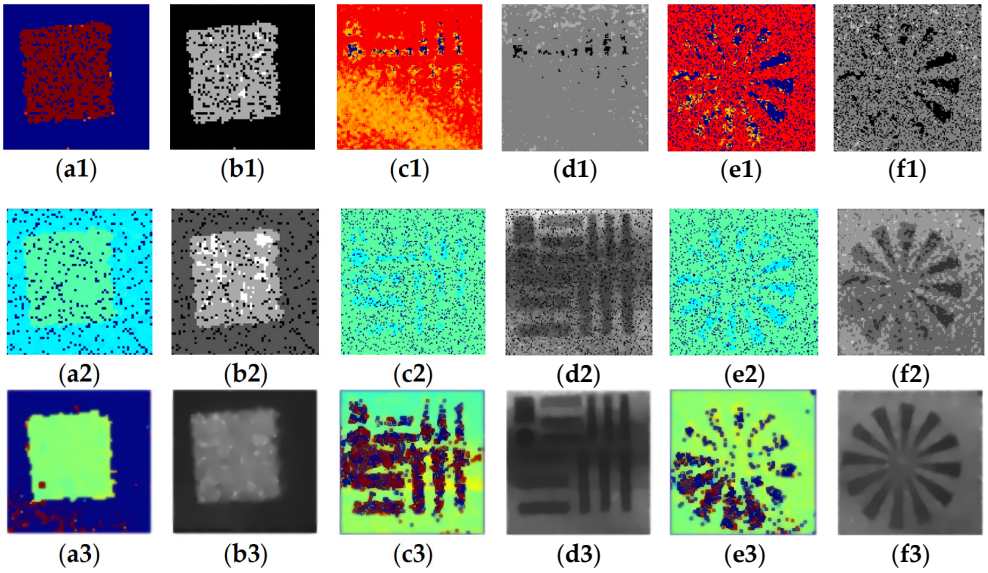


**Figure 21.** Results of the target reconstruction in the pipeline.

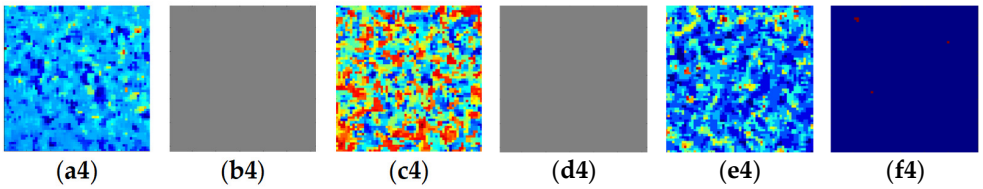


**Figure 22.** Imaging results under the inappropriate threshold of the first photon group algorithm.

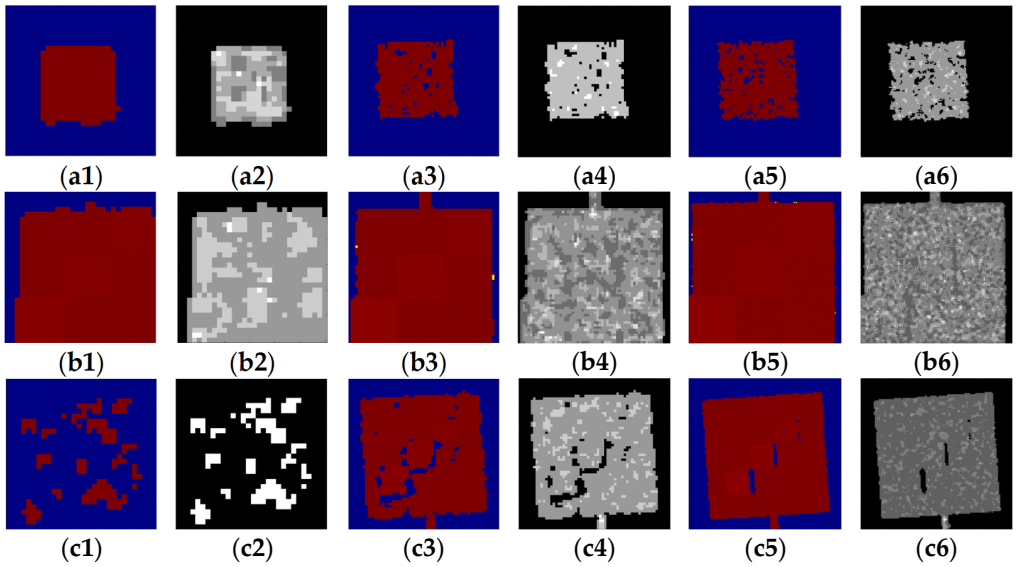


**Figure 23.** *Cont.*

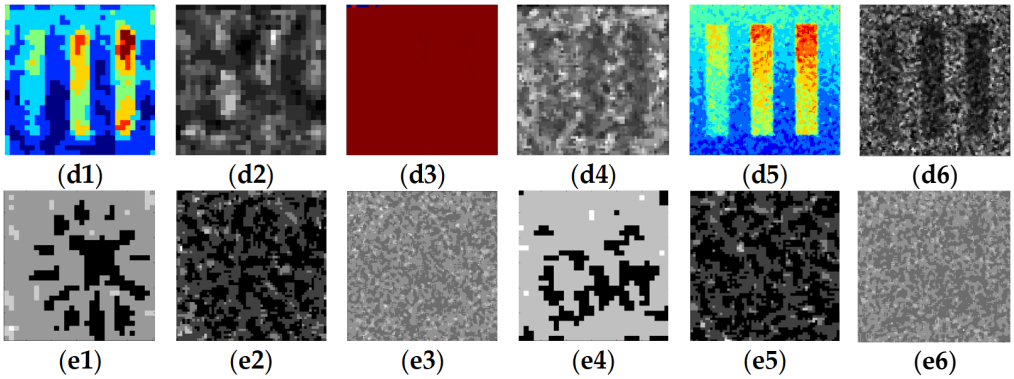


**Figure 23.** Image result of first photon group algorithm in the swimming pool.

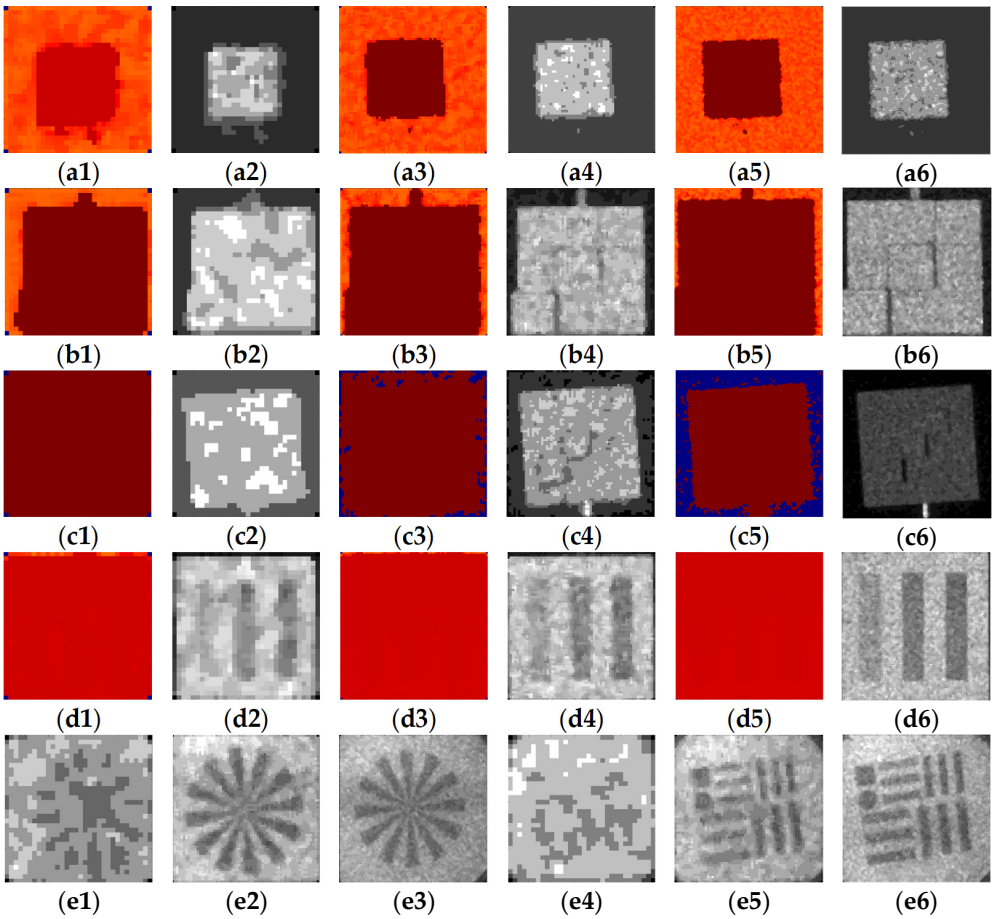


**Figure 24.** Image result of STMF algorithm in the swimming pool.

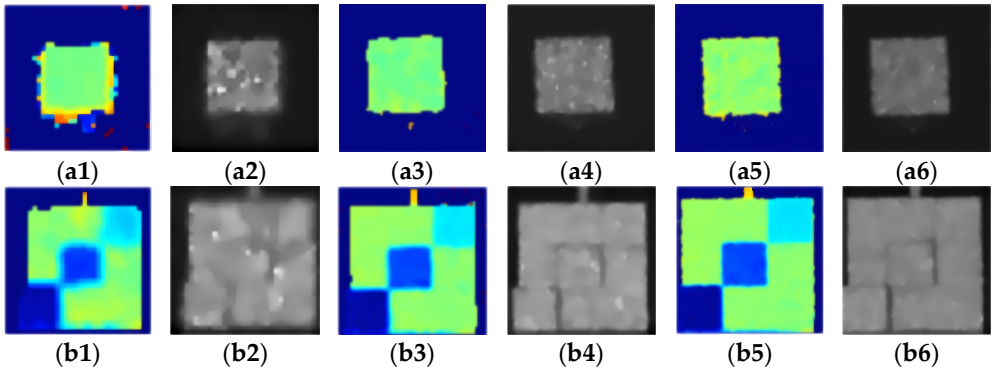


**Figure 25.** *Cont.*

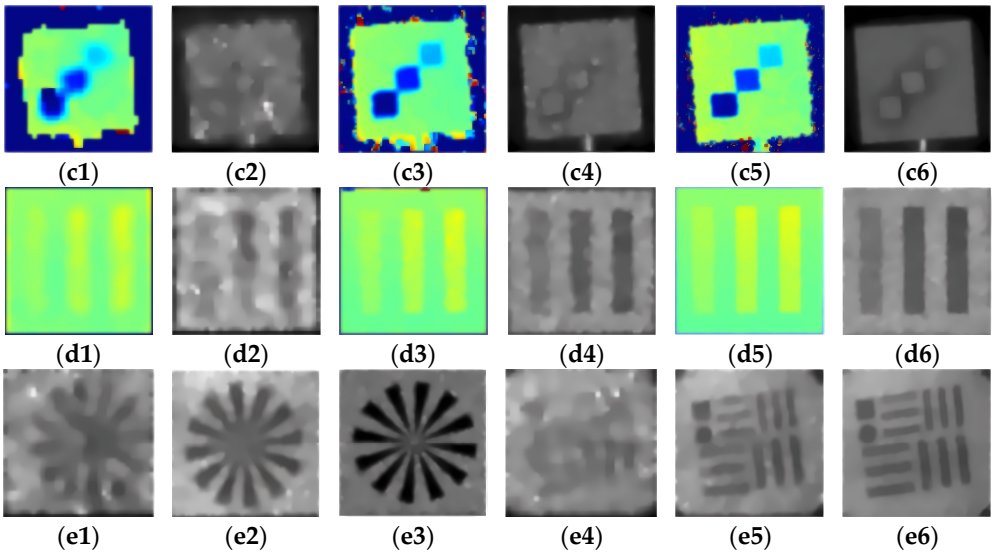


**Figure 25.** Image result of SUARF algorithm in the swimming pool.

Figures 23–25, (a) depict the depth maps and reflective intensity maps for the metal cube, (b) and (c) the depth maps and reflective intensity maps for the diagonal ladder distribution of metal blocks with different sizes for the base plate, (d) the depth maps and reflective intensity maps for the band target B, and (e) the depth maps and reflective intensity maps for the spoke-type target and band target B. In the above results, 1 and 2 are 32-pixel imaging result maps, 3 and 4 are 64-pixel imaging result maps, and 5 and 6 are 128-pixel imaging result maps. From the results of (a) metal cube, (b) diagonal ladder distribution of metal blocks, and (c) diagonal ladder distribution of metal blocks, the SUARF algorithm is superior to the first photon composition image algorithm and the STMF imaging algorithm in resolving deep targets. As can be seen from the results of (d) band target B and (e) spoke-type target and band target A, the SUARF algorithm still maintains a strong information extraction ability for different targets with the same depth. Moreover, the ability of the SUARF algorithm to smooth pixels is much better than the current first photon group image algorithm and the STMF imaging algorithm. Because the underwater test is difficult, it is not easy to keep the target stationary for a long time and observe the target with a large pulse number to obtain reference results; the above comparison results are easy to obtain intuitively, so we did not use indicators for evaluation, but direct observation. In order to further confirm the imaging advantages of the SUARF algorithm in the actual water environment, we conducted a comparative test on the imaging results of the actual water area, simultaneously, and the results are as follows.

In Figures 26–28, (a) and (b) depict the depth map and reflection intensity map for the metal cube, (c) and (d) the depth map and reflection intensity map for the spoke-type target, and (e) the depth map for the metal cube under a single detection pulse. From the reconstruction results in different water environments of Figures 21–28, it can be seen that in the challenging winter waters off the coast of China, the first-photon group image algorithm loses its stable imaging ability under laboratory conditions, and the STMF imaging algorithm has stronger information extraction ability than the first-photon group imaging algorithm. However, more complex spoke-type targets cannot be effectively imaged, especially in a single pulse, and information cannot be effectively extracted. Therefore, based on the imaging results in the pipeline, swimming pool, and actual waters, the SUARF algorithm proposed in this paper has stronger information extraction and outlier removal capabilities than the latest first-photon group and STMF imaging algorithms. It is able to accomplish the task well and achieve the detection of

small targets in all of the above water environments in which a lower number of detection pulses were used for detection. In the pipeline, because the wall of the tube compartment is very close to the target, it produces a large emission interference, which also simulates the detection of targets in narrow water areas. In the actual waters, after obtaining the single pulse data, the SUARF algorithm can also achieve more accurate detection of simple targets. On the basis of the obtained data, we also carried out a simulation analysis of the environmental influencing factors. We found that with the decrease of the signal-to-noise ratio (SNR), the RMSE value of SUARF imaging results gradually increased and the SSIM value gradually decreased, but it did not affect the observation of the scene contour, which reflects the algorithm's good underwater target reconstruction capability.

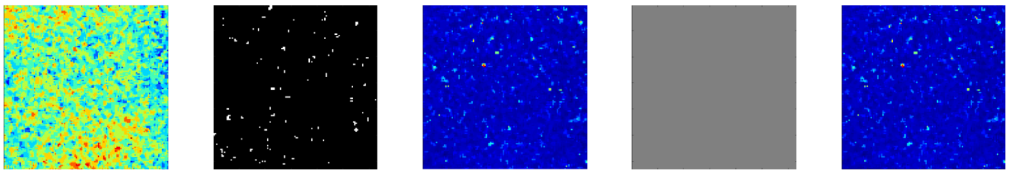


**Figure 26.** Imaging results of the first photon group algorithm in actual water off the coast of China.

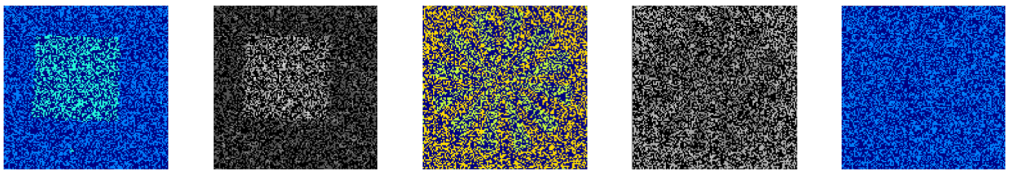


**Figure 27.** Imaging results of the STMF algorithm in actual water off the coast of China.

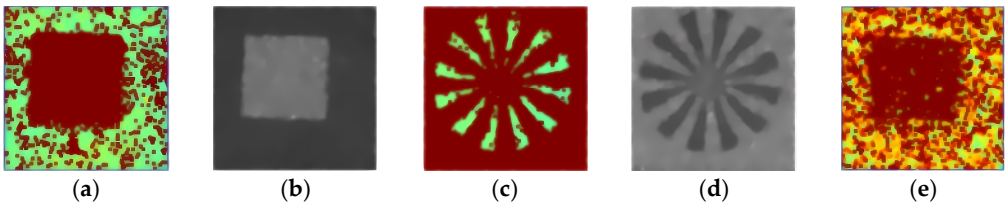


**Figure 28.** Imaging results of the SUARF algorithm in actual water off the coast of China.

## 5. Conclusions

This paper reports a sequential multimodal underwater single-photon lidar adaptive target reconstruction algorithm based on spatiotemporal sequence fusion, which consists of three steps: data preprocessing, sequence-optimized extreme value inference filtering, and collaborative variation strategy for image optimization. It has strong information extraction ability and noise filtering ability and can reconstruct target depth and reflection intensity information from complex echo photon time counts and spatial pixel relationships. The test results show that the SUARF algorithm utilizes the built single-photon lidar system to achieve underwater lateral resolution and distance resolution of 5 mm and 2.5cm@6AL, respectively, using a prototype constructed by ourselves, and it has stronger information extraction and compensation of anomalous pixel values compared to the currently available scanning single-photon lidar imaging algorithms. This effective target scene reconstruction algorithm endows underwater single-photon LiDAR with the ability to distinguish signal photons from noise photons in complex underwater environments and then realizes the imaging of small slow-moving underwater targets. It can depict the three-dimensional structure of historical relics such as shipwrecks and ruins in underwater archaeology, helping archaeologists explore the mysteries of ancient civilization. It can also be used in

the field of marine biological monitoring to capture marine organisms and habitats and provide intuitive data for biologists to study marine ecology. It can also detect the integrity and stability of key facilities such as submarine pipelines and bridge piers in underwater infrastructure testing to ensure the safe operation of marine engineering.

In future research, the system hardware facilities will be further analyzed to improve the hardware performance, the algorithm structure will be further optimized with the data results to provide a more optimized detection means for underwater target detection, and we will also design a complete environmental impact analysis experiment to evaluate the stability and adaptability of the algorithm under various environmental factors.

**Author Contributions:** Conceptualization, T.R.; methodology, T.R. and C.W.; software, T.R., C.W. and Q.L.; validation, T.R., Y.W. and Q.Z.; resources, C.W. and Z.Z.; data curation, T.R., Y.Z., J.L. and Y.W.; writing—original draft preparation, T.R.; writing—review and editing, T.R. and C.W.; project administration, C.W.; funding acquisition, C.W. All authors have read and agreed to the published version of the manuscript.

**Funding:** This research was funded by Key R&D Program of Shandong Province, China (Major Scientific and Technological Innovation Project), grant number 2022ZLGX04.

**Data Availability Statement:** All raw and processed data are available after publication by contacting the author.

**Acknowledgments:** I would like to thank my parents (Jianfang Liu and Yikun Rong), without their encouragement, it would have been difficult for me to have had firm confidence in my research. I also thank my girlfriend (Xiuyue Dong) for encouraging me in my research process.

**Conflicts of Interest:** The authors declare no conflicts of interest.

## References

1. Liu, B.; Liu, Z.; Men, S.; Li, Y.; Ding, Z.; He, J.; Zhao, Z. Underwater Hyperspectral Imaging Technology and Its Applications for Detecting and Mapping the Seafloor: A Review. *Sensors* **2020**, *20*, 4962. [CrossRef]
2. Song, Y.; Nakath, D.; She, M.; Köser, K. Optical Imaging and Image Restoration Techniques for Deep Ocean Mapping: A Comprehensive Survey. *PFG–J. Photogramm. Remote Sens. Geoinf. Sci.* **2022**, *90*, 243–267. [CrossRef]
3. Mills, M.S.; Ungermann, M.; Rigot, G.; den Haan, J.; Leon, J.X.; Schils, T. Assessment of the utility of underwater hyperspectral imaging for surveying and monitoring coral reef ecosystems. *Sci. Rep.* **2023**, *13*, 21103. [CrossRef] [PubMed]
4. Dumke, I.; Nornes, S.M.; Purser, A.; Marcon, Y.; Ludvigsen, M.; Ellefmo, S.L.; Johnsen, G.; Søreide, F. First hyperspectral imaging survey of the deep seafloor: High-resolution mapping of manganese nodules. *Remote Sens. Environ.* **2018**, *209*, 19–30. [CrossRef]
5. Gu, Z.; Liu, X.; Hu, Z.; Wang, G.; Zheng, B.; Watson, J.; Zheng, H. Underwater computational imaging: A survey. *Intell. Mar. Technol. Syst.* **2023**, *1*, 2. [CrossRef]
6. Chen, Y.; Guo, S.; He, Y.; Luo, Y.; Chen, W.; Hu, S.; Huang, Y.; Hou, C.; Su, S. Simulation and Design of an Underwater Lidar System Using Non-Coaxial Optics and Multiple Detection Channels. *Remote Sens.* **2023**, *15*, 3618. [CrossRef]
7. Daramola, O.; Nootz, G.; Britton, W. Fusion of AUV-Mounted 360-Degree Underwater LiDAR and Side Scan Sonar Data. In Proceedings of the OCEANS 2023—MTS/IEEE U.S. Gulf Coast, Biloxi, MS, USA, 25–28 September 2023; pp. 1–6. [CrossRef]
8. Shen, Y.; Zhao, C.; Liu, Y.; Wang, S.; Huang, F. Underwater Optical Imaging: Key Technologies and Applications Review. *IEEE Access* **2021**, *9*, 85500–85514. [CrossRef]
9. Churnside, J.H.; Shaw, J.A. Lidar remote sensing of the aquatic environment: Invited. *Appl. Opt.* **2020**, *59*, C92–C99. [CrossRef]
10. Hu, X. Underwater Image Enhancement Method Based on Wavelet Transform and Retinex. In Proceedings of the 2021 4th International Conference on Pattern Recognition and Artificial Intelligence (PRAI), Yibin, China, 20–22 August 2021; pp. 86–90. [CrossRef]
11. Junejo, N.U.R.; Sattar, M.; Adnan, S.; Sun, H.; Adam, A.B.M.; Hassan, A.; Esmaiel, H. A Survey on Physical Layer Techniques and Challenges in Underwater Communication Systems. *J. Mar. Sci. Eng.* **2023**, *11*, 885. [CrossRef]
12. Jekateryńczuk, G.; Piotrowski, Z. A Survey of Sound Source Localization and Detection Methods and Their Applications. *Sensors* **2024**, *24*, 68. [CrossRef]
13. Campo-Valera, M.; Diego-Tortosa, D.; Rodríguez-Rodríguez, I.; Useche-Ramírez, J.; Asorey-Cacheda, R. Signal Processing to Characterize and Evaluate Nonlinear Acoustic Signals Applied to Underwater Communications. *Electronics* **2024**, *13*, 4192. [CrossRef]

14. Lin, Z.; Shangguan, M.; Cao, F.; Yang, Z.; Qiu, Y.; Weng, Z. Underwater Single-Photon Lidar Equipped with High-Sampling-Rate Multi-Channel Data Acquisition System. *Remote Sens.* **2023**, *15*, 5216. [CrossRef]
15. Shangguan, M.; Yang, Z.; Lin, Z.; Lee, Z.; Xia, H.; Weng, Z. Compact Long-Range Single-Photon Underwater Lidar with High Spatial–Temporal Resolution. *IEEE Geosci. Remote Sens. Lett.* **2023**, *20*, 1501905. [CrossRef]
16. Yang, X.; Tong, Z.; Dai, Y.; Chen, X.; Zhang, H.; Zou, H.; Xu, J. 100 m full-duplex underwater wireless optical communication based on blue and green lasers and high sensitivity detectors. *Opt. Commun.* **2021**, *498*, 127261. [CrossRef]
17. Gao, Q.; Wang, C.; Wang, X.; Liu, Z.; Liu, Y.; Wang, Q.; Niu, W. Pointing Error Correction for Vehicle-Mounted Single-Photon Ranging Theodolite Using a Piecewise Linear Regression Model. *Sensors* **2024**, *24*, 3192. [CrossRef] [PubMed]
18. Degnan, J.J. Evolution of Single Photon Lidar: From Satellite Laser Ranging to Airborne Experiments to ICESat-2. *Photonics* **2024**, *11*, 924. [CrossRef]
19. Rapp, J.; Tachella, J.; Altmann, Y.; McLaughlin, S.; Goyal, V.K. Advances in Single-Photon Lidar for Autonomous Vehicles: Working Principles, Challenges, and Recent Advances. *IEEE Signal Process. Mag.* **2020**, *37*, 62–71. [CrossRef]
20. Hong, Y.; Liu, S.; Li, Z.P.; Huang, X.; Jiang, P.; Xu, Y.; Wu, C.; Zhou, H.; Zhang, Y.C.; Ren, H.L.; et al. Airborne single-photon LiDAR towards a small-sized and low-power payload. *Optica* **2024**, *11*, 612–618. [CrossRef]
21. Zhang, X.; Wang, F.; Guo, Y.; Wang, J.; Luo, Y.; Wu, W.; Hou, J.; Jiang, Z.; Peng, Z.; Huang, G.; et al. Research on linear array scanning lidar and photon signal processing technology based on InGaAs single-photon detector. *Infrared Laser Eng.* **2023**, *52*, 20220474. [CrossRef]
22. Shi, Y.; Li, Z.; Feng, B.; Yan, P.; Du, B.; Zhou, H.; Pan, H.; Wu, G. Enhanced solar-blind ultraviolet single-photon detection with a Geiger-mode silicon avalanche photodiode. *Chin. Opt. Lett.* **2016**, *14*, 030401. [CrossRef]
23. Xie, J.; Zhang, Z.; Jia, F.; Li, J.; Huang, M.; Zhao, Y. Improved single-photon active imaging through ambient noise guided missing data filling. *Opt. Commun.* **2022**, *508*, 127747. [CrossRef]
24. Zhang, H.; Zhao, X.; Zhang, Y.; Zhang, L.; Sun, M. Review of Advances in Single-Photon LiDAR. *Chin. J. Lasers* **2022**, *49*, 1910003. [CrossRef]
25. Li, Z.P.; Ye, J.T.; Huang, X.; Jiang, P.Y.; Cao, Y.; Hong, Y.; Yu, C.; Zhang, J.; Zhang, Q.; Peng, C.Z.; et al. Single-photon imaging over 200 km. *Optica* **2021**, *8*, 344–349. [CrossRef]
26. Signorelli, F.; Telesca, F.; Conca, E.; Della Frera, A.; Ruggeri, A.; Giudice, A.; Tosi, A. Low-Noise InGaAs/InP Single-Photon Avalanche Diodes for Fiber-Based and Free-Space Applications. *IEEE J. Sel. Top. Quantum Electron.* **2022**, *28*, 1–10. [CrossRef]
27. Tachella, J.; Altmann, Y.; Mellado, N.; McCarthy, A.; Tobin, R.; Buller, G.S.; Tourneret, J.Y.; McLaughlin, S. Real-time 3D reconstruction from single-photon lidar data using plug-and-play point cloud denoisers. *Nat. Commun.* **2019**, *10*, 4984. [CrossRef]
28. Caramazza, P.; Boccolini, A.; Buschek, D.; Hullin, M.; Higham, C.F.; Henderson, R.; Murray-Smith, R.; Faccio, D. Neural network identification of people hidden from view with a single-pixel, single-photon detector. *Sci. Rep.* **2018**, *8*, 11945. [CrossRef]
29. Ma, L.; Sun, J.; Yang, X.; Lu, J.; Lu, W.; Zhou, X.; Ni, H. Reconstruction method of 128 × 256 array single photon Lidar based on multi-domain stability feature fusion. *Opt. Laser Technol.* **2025**, *181 Pt C*, 111970. [CrossRef]
30. Halimi, A.; Tobin, R.; McCarthy, A.; McLaughlin, S.; Buller, G.S. Restoration of Multilayered Single-Photon 3D Lidar Images. In Proceedings of the 2018 IEEE 10th Sensor Array and Multichannel Signal Processing Workshop (SAM), Sheffield, UK, 8–11 July 2018; pp. 642–646. [CrossRef]
31. Bian, L.; Song, H.; Peng, L.; Chang, X.; Yang, X.; Horstmeyer, R.; Ye, L.; Zhu, C.; Qin, T.; Zheng, D.; et al. High-resolution single-photon imaging with physics-informed deep learning. *Nat. Commun.* **2023**, *14*, 5902. [CrossRef] [PubMed]
32. Zhao, X.; Wu, M.; Zhang, Y.; Wang, C.; Chen, R.; He, W.; Chen, Q. Robust single-photon 3D imaging based on full-scale feature integration and intensity edge guidance. *Opt. Lasers Eng.* **2024**, *172*, 107850. [CrossRef]
33. Cai, R.; Guo, H.; Li, X.; Che, J.; He, J.; Liu, H.; Yang, L.; Guo, Y.; Pu, M.; Luo, X. Sub-diffraction-limited single-photon 3D imaging based on domain features extraction network at kilometer-scale distance. *Opt. Laser Technol.* **2025**, *181 Pt B*, 111868. [CrossRef]
34. Xia, F.; Kim, K.; Eliezer, Y.; Shaughnessy, L.; Gigan, S.; Cao, H. Deep Learning with Passive Optical Nonlinear Mapping. *arXiv* **2024**, arXiv:2307.08558. [CrossRef]
35. Bosse, S.; Maniry, D.; Müller, K.R.; Wiegand, T.; Samek, W. Deep Neural Networks for No-Reference and Full-Reference Image Quality Assessment. *IEEE Trans. Image Process.* **2018**, *27*, 206–219. [CrossRef] [PubMed]
36. Wang, Z.; Chen, J.; Hoi, S.C. Deep Learning for Image Super-Resolution: A Survey. *IEEE Trans. Pattern Anal. Mach. Intell.* **2021**, *43*, 3365–3387. [CrossRef] [PubMed]
37. Xu, Y.; Tong, Z.; Jiang, P.; Xu, L.; Wu, L.; Hu, J.; Yang, C.; Zhang, W.; Zhang, Y.; Zhang, J.; et al. Deep-learning based photon-efficient 3D and reflectivity imaging with a 64 × 64 single-photon avalanche detector array. *Opt. Express* **2022**, *30*, 32948–32964. [CrossRef]
38. Shao, W.; Rowe, S.P.; Du, Y. Artificial intelligence in single photon emission computed tomography (SPECT) imaging: A narrative review. *Ann. Transl. Med.* **2021**, *9*, 820. [CrossRef]
39. Yao, D.; Yang, C.; Li, H. PCA-based real-time single-photon 3D imaging method. *Opt. Commun.* **2022**, *508*, 127777. [CrossRef]

40. Zhu, G.; Nan, Z.; Zhang, X.; Chu, K.; Zhan, S.; Liu, X.; Lin, X. High anti-interference 3D imaging LIDAR system based on digital chaotic pulse position modulation. *Opt. Laser Technol.* **2023**, *163*, 109405. [CrossRef]
41. Xu, R.; Ye, H.; Lv, H.; Sun, J.; Shi, Y.; Liu, W.; Zhao, T.; Song, Y. Single-photon lidar depth imaging based on sparsity adaptive matching pursuit method. *Opt. Lasers Eng.* **2024**, *180*, 108314. [CrossRef]
42. Kirmani, A.; Venkatraman, D.; Shin, D.; Colaço, A.; Wong, F.N.C.; Shapiro, J.H.; Goyal, V.K. First-Photon Imaging. *Science* **2013**, *343*, 58–61. [CrossRef]
43. Peng, X.; Zhao, X.Y.; Li, L.J.; Sun, M.J. First-photon imaging via a hybrid penalty. *Photonics Res.* **2020**, *8*, 325–330. [CrossRef]
44. Hua, K.; Liu, B.; Wang, H.; Fang, L.; Chen, Z.; Luo, J. Efficient and noise robust photon-counting imaging method. In Proceedings of the Seventh Symposium on Novel Photoelectronic Detection Technology and Applications, Kunming, China, 5–7 November 2020; 117632H. SPIE: Bellingham, WC, USA, 2021; Volume 11763. [CrossRef]
45. Hua, K.; Liu, B.; Chen, Z.; Fang, L.; Wang, H. Efficient and Noise Robust Photon-Counting Imaging with First Signal Photon Unit Method. *Photonics* **2021**, *8*, 229. [CrossRef]
46. Goudreault, F.; Scheuble, D.; Bijelic, M.; Robidoux, N.; Heide, F. LiDAR-in-the-Loop Hyperparameter Optimization. In Proceedings of the IEEE/CVF Conference on Computer Vision and Pattern Recognition (CVPR), Vancouver, BC, Canada, 17–24 June 2023; pp. 13404–13414. [CrossRef]
47. Liu, X.; Shi, J.; Chen, H.; Zeng, G. First-Photon Ghost Imaging at Low Light Level. In Proceedings of the Conference on Lasers and Electro-Optics, OSA Technical Digest (online) (Optica Publishing Group 2017), San Jose, CA, USA, 4–19 May 2017; pp. 1–2. Available online: https://ieeexplore.ieee.org/document/8082923 (accessed on 26 November 2024).
48. Xu, Y.; Jiang, X.; Jiang, P.; Xu, L.; Wu, L.; Hu, J.; Zhang, Y.; Zhang, J.; Zou, B. S2O-FSPI: Fourier single pixel imaging via sampling strategy optimization. *Opt. Laser Technol.* **2023**, *166*, 109651. [CrossRef]
49. Rong, T.; Wang, Y.; Zhu, Q.; Wang, C.; Zhang, Y.; Li, J.; Zhou, Z.; Luo, Q. Sequential Two-Mode Fusion Underwater Single-Photon Lidar Imaging Algorithm. *J. Mar. Sci. Eng.* **2024**, *12*, 1595. [CrossRef]
50. Draz, H.H.; Elashker, N.E.; Mahmoud, M.M.A. Optimized Algorithms and Hardware Implementation of Median Filter for Image Processing. *Circuits Syst. Signal Process.* **2023**, *42*, 5545–5558. [CrossRef]
51. Lone, M.R.; Sandhu, A.K. Enhancing image quality: A nearest neighbor median filter approach for impulse noise reduction. *Multimed. Tools Appl.* **2024**, *83*, 56865–56881. [CrossRef]
52. Shin, D.; Kirmani, A.; Goyal, V.K.; Shapiro, J.H. Photon-Efficient Computational 3-D and Reflectivity Imaging with Single-Photon Detectors. *IEEE Trans. Comput. Imaging* **2015**, *1*, 112–125. [CrossRef]
53. Rapp, J.; Goyal, V. A Few Photons Among Many: Unmixing Signal and Noise for Photon-Efficient Active Imaging. *IEEE Trans. Comput. Imaging* **2017**, *3*, 445–459. [CrossRef]
54. Maccarone, A.; Drummond, K.; McCarthy, A.; Steinlehner, U.K.; Tachella, J.; Garcia, D.A.; Pawlikowska, A.; Lamb, R.A.; Henderson, R.K.; McLaughlin, S.; et al. Submerged single-photon LiDAR imaging sensor used for real-time 3D scene reconstruction in scattering underwater environments. *Opt. Express* **2023**, *31*, 16690–16708. [CrossRef] [PubMed]
55. Noether, F. Über eine Klasse singulärer Integralgleichungen. *Math. Ann.* **1920**, *82*, 42–63. [CrossRef]
56. Döttling, M.; Mohr, W.; Osseiran, A. WINNER II Channel Models. In *Radio Technologies and Concepts for IMT-Advanced*; Wiley: Hoboken, NJ, USA, 2010; pp. 39–92. [CrossRef]
57. Chan, S.H.; Khoshabeh, R.; Gibson, K.B.; Gill, P.E.; Nguyen, T.Q. An augmented Lagrangian method for total variation video restoration. *IEEE Trans. Image Process.* **2011**, *20*, 3097–3111. [CrossRef] [PubMed]
58. Wang, X.; Xie, L.; Dong, C.; Shan, Y. Real-ESRGAN: Training Real-World Blind Super-Resolution with Pure Synthetic Data. In Proceedings of the 2021 IEEE/CVF International Conference on Computer Vision Workshops (ICCVW), Montreal, BC, Canada, 11–17 October 2021; pp. 1905–1914. [CrossRef]
59. Wang, Z.; Bovik, A.C.; Sheikh, H.R.; Simoncelli, E.P. Image quality assessment: From error visibility to structural similarity. *IEEE Trans. Image Process.* **2004**, *13*, 600–612. [CrossRef] [PubMed]
60. Estévez, J.; Bellido-Jiménez, J.A.; Liu, X.; García-Marín, A.P. Monthly Precipitation Forecasts Using Wavelet Neural Networks Models in a Semiarid Environment. *Water* **2020**, *12*, 1909. [CrossRef]